

## Data-driven Dynamics with Orbital Torus Imaging: A Flexible Model of the Vertical Phase Space of the Galaxy

ADRIAN M. PRICE-WHELAN,<sup>1</sup> JASON A. S. HUNT,<sup>1,2</sup> DANNY HORTA,<sup>1</sup>  
MICAH OEUR,<sup>3</sup> DAVID W. HOGG,<sup>1,4,5</sup> KATHRYN JOHNSTON,<sup>6</sup> AND  
LAWRENCE WIDROW<sup>7</sup>

<sup>1</sup> *Center for Computational Astrophysics, Flatiron Institute,  
162 Fifth Ave, New York, NY 10010, USA*

<sup>2</sup> *School of Mathematics & Physics, University of Surrey, Guildford, GU2 7XH, UK*

<sup>3</sup> *Department of Physics, University of California, Merced,  
5200 Lake Road, Merced, CA 95343, USA*

<sup>4</sup> *Max-Planck-Institut für Astronomie, Königstuhl 17, D-69117 Heidelberg, Germany*

<sup>5</sup> *Center for Cosmology and Particle Physics, Department of Physics, New York University,  
726 Broadway, New York, NY 10003, USA*

<sup>6</sup> *Department of Astronomy, Columbia University, 550 West 120th Street, New York, NY 10027, USA*

<sup>7</sup> *Department of Physics, Engineering Physics and Astronomy, Queen’s University,  
Kingston, K7L 3X5, Canada*

### ABSTRACT

The vertical kinematics of stars near the Sun can be used to measure the total mass distribution near the Galactic disk and to study out-of-equilibrium dynamics. With contemporary stellar surveys, the tracers of vertical dynamics are so numerous and so well measured that the shapes of underlying orbits are almost directly visible in the data through element abundances or even stellar density. These orbits can be used to infer a mass model for the Milky Way, enabling constraints on the dark matter distribution in the inner galaxy. Here we present a flexible model for foliating the vertical position–velocity phase space with orbits, for use in data-driven studies of dynamics. The vertical acceleration profile in the vicinity of the disk, along with the orbital actions, angles, and frequencies for individual stars, can all be derived from that orbit foliation. We show that this framework — “Orbital Torus Imaging” (OTI) — is rigorously justified in the context of dynamical theory, and does a good job of fitting orbits to simulated stellar abundance data with varying degrees of realism. OTI (1) does not require a global model for the Milky Way mass distribution, and (2) does not require detailed modeling of the selection function of the input survey data. We discuss the approximations and limitations of the OTI framework, which currently trades dynamical interpretability for flexibility in representing the data in some regimes, and which also presently separates the vertical and radial dynamics. We release an open-source tool, `torusimaging`, to accompany this article.

## 1. INTRODUCTION

The distribution of mass in the Milky Way is key to many of the questions of astrophysics. For one, the mass density determines the orbits of its gas, stars, star clusters, and satellite galaxies, and thus enables interpreting the kinematic snapshot we observe in terms of dynamical and galactic evolutionary processes (e.g., [Freeman & Bland-Hawthorn 2002](#); [Helmi 2020](#)). For another, the distribution of mass depends on the properties of the dark matter on the scale of an individual galaxy (e.g., [Bertone et al. 2005](#); [Buckley & Peter 2018](#)), which in turn has implications for fundamental physics and the cosmological model. On Galaxy mass scales (and smaller), effective models for dark matter predict different density profiles and different populations of substructures (e.g., [Bullock & Boylan-Kolchin 2017](#)). Precise measurements of the dark matter within the Milky Way and other nearby galaxies therefore constrain the particle nature of dark matter. As a last example, the phase-space distribution function of stars encodes, at some level, the assembly history of the Galaxy (e.g., [Helmi et al. 2018](#); [Belokurov et al. 2018](#)), and thus the initial conditions of the primordial patch that evolved into our home in the Universe (e.g., [Peebles et al. 2011](#)).

Until direct measurements of the Galactic acceleration field become more ubiquitous ([Gaia Collaboration et al. 2021](#); [Chakrabarti et al. 2021](#)), our best hope for studying the mass and dark matter content of the Milky Way comes from modeling stellar kinematics (e.g., [Oort 1932](#); [Binney & Tremaine 2008](#); [Rix & Bovy 2013](#)). The principal challenge of this problem is that we only observe a *snapshot* of the kinematics (i.e. position  $\boldsymbol{x}$  and velocity  $\boldsymbol{v}$ ) of stars throughout the Galaxy at present day. We do not observe the orbits of stars or even segments of their orbits, which would enable a more direct measurement of the acceleration field around those orbits. Instead, we have to rely on statistical mechanics to relate the snapshot of tracer kinematics we observe to the underlying mass distribution (e.g., [Kuijken & Gilmore 1989a](#); [Binney & Tremaine 2008](#); [Magorrian 2014](#)).

Contemporary stellar surveys provide kinematic data for millions to billions of stars throughout our Galaxy. These surveys have enabled new views of the Milky Way that extend far beyond the solar neighborhood, and have opened up new dimensions for studying the stellar populations of the Milky Way by providing high-quality stellar labels (e.g., element abundances, ages, masses, etc.) for large samples of stars. This includes the transformative astrometric, photometric, and spectroscopic data from the *Gaia* Mission ([Gaia Collaboration et al. 2016, 2023](#)), deep, multi-band photometric surveys such as the Sloan Digital Sky Survey (SDSS; [York et al. 2000](#)), Dark Energy Survey (DES; [Dark Energy Survey Collaboration et al. 2016](#)), and high-resolution spectroscopic surveys such as the Apache Point Observatory Galactic Evolution Experiment (APOGEE; [Majewski et al. 2017](#)). Many other stellar surveys are currently underway or planned for the near future that will expand (or are expanding) the spatial volume, number of stars, number of measured properties, and precision of the available data for Milky Way stars, such as LAMOST ([Yan et al. 2022](#)), GALAH ([De Silva et al. 2015](#); [Buder et al. 2022](#)), WEAVE ([Jin et al. 2023](#)), 4MOST ([de Jong et al. 2019](#)), SDSS-V ([Kollmeier et al. 2017](#)), and the Rubin observatory

LSST (LSST Science Collaboration et al. 2009). This wealth of stellar survey data presently available brings an opportunity to make precise measurements of the detailed structure of matter and dark matter throughout the Milky Way and learn about its formation history by combining stellar label and kinematic data.

Near-invariant stellar labels are complementary to measurements of phase-space dimensions and can serve as invariant tracers that provide important information in dynamical analyses. This idea has already been used and exploited in many contexts. For example, additional stellar labels can be added in to the phase-space distribution function (DF) explicitly to form an “extended distribution function” (eDF)  $f(\mathbf{W}, \mathbf{Y})$  (e.g., Sanders & Binney 2015; Binney & Vasiliev 2023), where here the vector  $\mathbf{W}$  represents the kinematic information (i.e. positions and velocities, or integrals of motion) and  $\mathbf{Y}$  represents any stellar labels, like element abundances. This is a powerful approach because it allows for using the stellar labels to help in the dynamical inference of the mass distribution, but requires making choices about how to parameterize the form of the eDF and any correlations between the kinematics and stellar labels. Another challenge with this approach is that it requires a model for the selection function of the survey to accurately infer the DF properties, which is often not modeled at a high enough precision to handle the model flexibility demanded by present data.

A different approach has been to model and study the conditional distribution  $f(\mathbf{W} | \mathbf{Y})$ . When  $\mathbf{Y}$  represents element abundances, these are called “mono-abundance populations” (Bovy et al. 2012, 2016). This approach is useful because it is conditional on the stellar labels and therefore does not necessarily require explicitly parameterizing the relationship between the kinematics and stellar labels (e.g., one can bin in the parameters  $\mathbf{Y}$  and study the kinematic DF in those bins). However, this still requires parameterizing the form of the DF in the kinematic dimensions, and using a model for the selection function of the survey.

We previously introduced a third approach that involves modeling the complementary factorization  $f(\mathbf{Y} | \mathbf{W})$ , which we call “Orbital Torus Imaging” (OTI; Price-Whelan et al. 2021). This approach does not require detailed knowledge of the survey selection function in terms of kinematic quantities as long as there is no strong joint dependence on kinematics and stellar labels. That is, the selection function  $S$  should be approximately separable in kinematic quantities and stellar labels such that  $S = S(\mathbf{W}) S(\mathbf{Y})$ . OTI is therefore more robust to spatial selection effects than the eDF or mono-abundance population approaches to modeling Milky Way disk kinematics. However, it does still require parameterizing any relationships between the kinematics and stellar labels.

In this work, motivated by the need for flexible dynamical inference methods that make fewer assumptions about the form of the potential and DF, we build off of the OTI framework to outline an approach that only requires modeling the shapes of orbits in projections of phase space. A companion paper uses this modeling framework to measure the acceleration field and properties of the Milky Way disk without assuming a global model for the Galactic potential (Horta et al. 2023).

## 2. REVIEW OF VERTICAL DYNAMICS IN AN AXISYMMETRIC DISK

Our goal, like many past efforts, is to define a path for measuring the mass distribution underlying a tracer population given a snapshot of kinematic data for the tracers. For this work, we will consider stars as the tracers and the particular case of modeling the mass distribution around the Milky Way disk, but we note that these ideas are generalizable to other contexts. Though our eventual hope is to build a method that can handle time dependence and disequilibrium, we will start with a set of standard assumptions to simplify the setup and limit the dimensionality of expressions. In particular, for now we will assume that the Galaxy is in equilibrium, that the distribution function (DF) is in steady state, that the system is axisymmetric, and that orbital motion is separable in cylindrical radius  $R$  and vertical position  $z$ . That is, we assume that the total gravitational potential  $\Phi$  is additively separable such that

$$\Phi(R, z) \approx \Phi_R(R) + \Phi_z(z) \quad . \quad (1)$$

This is a typical assumption for near-circular orbits in an axisymmetric potential, such as for stellar populations within the Galactic disk.

Under the assumptions stated above, the orbits in such a system are governed by a gravitational acceleration field  $\mathbf{a}(R, z)$  that is related to the underlying mass density  $\rho$  through Poisson's equation,

$$\frac{1}{R} \frac{\partial}{\partial R} (R a_R) + \frac{\partial a_z}{\partial z} = -4\pi G \rho(R, z) \quad (2)$$

where  $\mathbf{a} = -\nabla\Phi$  is the acceleration. If we assume that we will always work in a small annular volume (i.e. a small range of  $R$ ), and that the circular velocity curve as a function of radius  $v_c(R)$  is nearly flat over the volume considered, then the radial gradient in the left hand side will be small and can be neglected, leaving only the vertical terms

$$-\left. \frac{\partial a_z}{\partial z} \right|_R = 4\pi G \rho_z(z; R) \quad (3)$$

where the expressions are assumed to be valid at a given radius  $R$ . Very near the galactic midplane, the mass density distribution is approximately constant,

$$\rho(z \approx 0) \approx \rho_0 \rightarrow a_z(z) \approx -4\pi G \rho_0 z \quad (4)$$

so the shapes of orbits in the vertical phase space are close to ellipses with an aspect ratio set by the asymptotic midplane vertical frequency,

$$\Omega_0^2 = 4\pi G \rho_0 \quad . \quad (5)$$

Orbits that stray further from the midplane will feel an anharmonic potential such that the vertical frequency decreases for orbits that reach successively higher maximum heights,  $z_{\text{max}}$ . See [Read \(2014\)](#) for a review of mass-modeling methods that use the vertical kinematics of stars to infer the vertical density or surface mass density structure of the Milky Way (see also, e.g., [Widmark & Monari 2019](#); [Buch et al. 2019](#); [Widmark et al. 2021](#); [Li & Widrow 2021](#), for recent work on the vertical dynamics of the disk).

Orbits in generic axisymmetric, equilibrium systems permit three integrals of motion that are useful for summarizing and labeling the orbits. For example, the energy  $E$ ,  $z$ -component of angular momentum  $L_z$ , and the “third integral”  $I_3$  are all conserved quantities for orbits in an axisymmetric disk. A more useful set of integrals of motion are the orbital actions  $\mathbf{J} = (J_R, J_\phi, J_z)$  (Binney & Tremaine 2008). Actions are independent isolating integrals of motion that are special in that they are also the momentum coordinates of a set of canonical coordinates known as action–angle coordinates. In this coordinate system, the angle variables  $\boldsymbol{\theta}$  are the conjugate position coordinates that increase linearly with time with a rate set by the orbital frequencies  $\boldsymbol{\Omega}$ .

For this work, as mentioned above, we will consider only the vertical phase space of the Galaxy under the assumption that the radial and vertical motion are separable (see also, e.g., Oort 1932; Bahcall 1984; Kuijken & Gilmore 1989b, 1991; Holmberg & Flynn 2000; Li & Widrow 2021; Green et al. 2023). Orbits in the vertical phase space are then fully summarized by the vertical action  $J_z$ , and the phase of a star along its orbit is set by the vertical angle  $\theta_z$ . The vertical action is defined as the area that an orbit sweeps out in the vertical phase space, i.e.,

$$J_z = \frac{1}{2\pi} \oint dz v_z(z) \quad , \quad (6)$$

where this integral is done over a full orbital path, which is a closed curve in the vertical phase space under our assumptions. Another important invariant property of orbits is the vertical frequency  $\Omega_z$ , which is related to the vertical period of an orbit  $T_z = 2\pi/\Omega_z$ . The vertical period can be computed as

$$T_z = \oint \frac{dz}{v_z(z)} \quad (7)$$

where the integral is again done over the orbital path. In general, the vertical frequency and period of an orbit depends on its action  $\Omega_z = \Omega_z(J_z)$ .

### 3. ORBITAL TORUS IMAGING

The orbital actions  $\mathbf{J}$  are useful quantities for summarizing orbits and constructing dynamical models. However, they require a global model for the gravitational potential, are expensive to compute, and are not directly observable. This makes action-based dynamical modeling methods computationally challenging to apply to large samples and restrictive in terms of the flexibility of the potential model. Fortunately, for increasingly large samples of stars in the Milky Way, we have access to measurements of intrinsic, invariant stellar labels, such as stellar surface element abundance ratios or stellar ages. These stellar labels can be used instead to trace out the orbit structure of the Galaxy. This forms the basis of the method of Orbital Torus Imaging (OTI; Price-Whelan et al. 2021), which we describe below. Here we build on past work by rigorously justifying the method and developing a new implementation of OTI that leverages modern auto-differentiation tools (e.g., JAX; Bradbury et al. 2018) to generalize and accelerate the model construction and fitting.

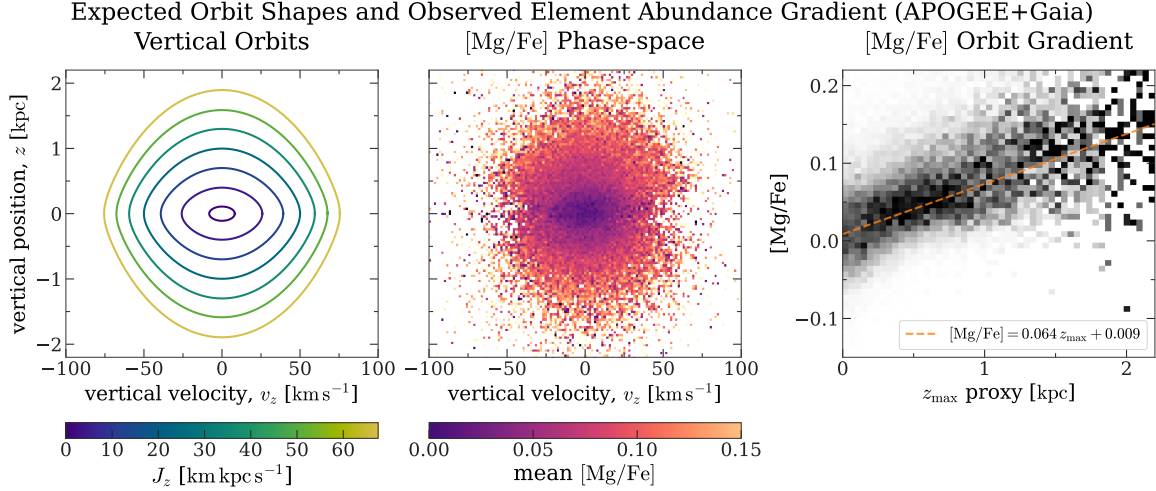


**Figure 1.** A demonstration that stellar labels correlate with stellar orbits in the vertical phase space of the Milky Way disk. **Left panel:** Seven orbits computed in a Milky Way mass model (see Appendix A) and shown in the vertical phase space,  $(z, v_z)$ . The orbits have equally-spaced values of the maximum height above the midplane each orbit reaches,  $z_{\max}$ . The vertical action,  $J_z$ , of these orbits scales approximately like  $J_z \propto z_{\max}^2$ , and all orbits have  $J_R = 0$  and  $J_\phi \approx 1900 \text{ km s}^{-1} \text{ kpc}$ . **Middle panel:** The mean  $[\text{Mg}/\text{Fe}]$  abundance for stars in the low- $\alpha$  sequence and with angular momenta  $L_z$  within  $\pm 15\%$  of the value for a circular orbit at the Sun’s position ( $L_{z,c} \approx 1900$ ). The mean  $[\text{Mg}/\text{Fe}]$  abundance is shown in small bins of the vertical position,  $z$ , and velocity,  $v_z$ . The mean abundance is systematically different for stars with low vertical action  $J_z$  (i.e. near  $(z, v_z) \sim (0, 0)$ ) as compared to stars with larger vertical action. **Right panel:** The column-normalized density of stars in  $[\text{Mg}/\text{Fe}]$  as a function of an observable proxy for  $z_{\max}$ . We estimate a proxy for  $z_{\max}$  for the data *without using a potential model* by selecting only stars with  $|v_z| < 10 \text{ km s}^{-1}$  (i.e. stars that are near their vertical apocenter). The over-plotted dashed (orange) line shows a linear relation between  $[\text{Mg}/\text{Fe}]$  and  $z_{\max}$ .

### 3.1. Using stellar labels to map orbits

Stars have a number of observable properties that are approximately invariant over their lifetimes, or at least over galactic orbital timescales. For example, the surface element abundance ratios, birth time (as a time-invariant proxy of age), and stellar mass, to name a few. We represent these quantities with the vector  $\mathbf{Y}$ , which we refer to as the “stellar labels”. In the Milky Way, these quantities are observed to correlate with the orbital properties of stellar populations. For example, there is a long known correlation between stellar age and velocity dispersion (Spitzer & Schwarzschild 1951; Sharma et al. 2021), the kinematic properties of mono-abundance stellar populations depend on the value of the abundance (Bovy et al. 2016; Yu et al. 2021; Lian et al. 2022), and there are known gradients in element abundances and Galactic position (e.g., Shaver et al. 1983; Maciel & Quireza 1999; Eilers et al. 2022; Lian et al. 2023). Figure 1 shows an example of such a correlation in the vertical kinematics of stars in the Milky Way. The left panel of Figure 1 shows seven orbits in the vertical phase space (with  $J_R = 0$  and  $J_\phi \approx 1900 \text{ km s}^{-1} \text{ kpc}$ ), with equally-spaced values of  $z_{\max}$  as computed in a Milky Way-like gravitational potential around the solar position (see Section A). The vertical action scales approximately with  $J_z \approx \frac{1}{2} \Omega_z z_{\max}^2$ . The middle panel shows the mean  $[\text{Mg}/\text{Fe}]$  abundance (as measured by the APOGEE surveys,

DR17; Majewski et al. 2017; Abdurro’uf et al. 2022) for stars in different locations of the vertical phase space. This demonstrates that stars with low- $J_z$  orbits (i.e. those that stay near the center of this phase space) have systematically different element abundances than stars with large- $J_z$  orbits (i.e. those that stay far from the center of this phase space).

Under the assumptions listed in Section 2, the correlations between any intrinsic, time-invariant stellar properties  $\mathbf{Y}$  and the orbital properties of stars can only depend on the orbital actions  $\mathbf{J}$  and not the angles  $\boldsymbol{\theta}$ , which are time dependent. This is useful because it means we can use the stellar labels as constants of motion themselves to trace out the shapes of orbits in phase space. In the context of vertical dynamics, the vertical action  $J_z$  is, by construction, constant along an orbit, so any time-invariant function of the vertical action is also constant along an orbit.

With a suitably large sample of stars, this provides a means to measure the orbital structure and acceleration field of the Galaxy directly, without having to assume a form for the potential and without needing to compute the actions. As long as the gradient in stellar labels as a function of vertical action  $\frac{dY}{dJ_z}$  is non-zero (i.e. not flat), we can use the level sets of constant stellar label  $Y$  to “contour” the orbits in the vertical phase space  $(z, v_z)$ .<sup>1</sup> In reality, the stellar labels are not deterministic functions of the action or of the vertical phase space: There is a distribution of abundance values at any location of the phase space  $p_Y(Y | z, v_z)$ , as is apparent in Figure 1. This is expected, given that the processes that induce correlations between the vertical action, stellar age, and metallicity are inherently stochastic (Nordström et al. 2004; Hayden et al. 2022). We will show, however, that moments of the stellar label distribution at different locations of phase space still enable us to contour the orbits because the distribution of abundances changes across the vertical phase space.

To see this, we define the (steady-state) extended distribution function (eDF)  $\mathcal{F}$  of the vertical phase space and stellar label  $Y$  as

$$\mathcal{F}(z, v_z, Y) = f(z, v_z) p_Y(Y | z, v_z) \quad (8)$$

where  $f(z, v_z)$  is the distribution function (DF) and  $p_Y(Y | z, v_z)$  is the distribution of stellar labels at each location in phase space. The DF necessarily satisfies the collisionless Boltzmann equation (CBE; see, e.g., Binney & Tremaine 2008), assuming stars are not created or destroyed, which is a statement of the continuity equation for the phase-space density  $f$ :

$$\frac{Df}{Dt} = 0 \quad (9)$$

$$0 = \cancel{\frac{\partial f}{\partial t}} + \dot{z} \frac{\partial f}{\partial z} + \dot{v}_z \frac{\partial f}{\partial v_z} \quad (10)$$

$$= v_z \frac{\partial f}{\partial z} - \frac{d\Phi}{dz} \frac{\partial f}{\partial v_z} \quad (11)$$

<sup>1</sup> We note that this idea, in the context of using the phase-space density as a stellar label, was briefly discussed in Kuijken & Gilmore (1989a) and referred to as “direct contouring” of the DF. This has been implemented and used previously with parametric models of the DF and potential to study the vertical dynamics Li & Widrow (2021, 2023).

where  $\dot{x} = \frac{dx}{dt}$ . The eDF  $\mathcal{F}$  also satisfies a continuity equation: Defining the vector  $\mathbf{w} = (z, v_z, Y)$ , we have

$$\frac{\partial \mathcal{F}}{\partial t} + \frac{\partial}{\partial \mathbf{w}} \cdot (\mathcal{F} \dot{\mathbf{w}}) = 0 \quad (12)$$

$$\frac{\partial}{\partial \mathbf{w}} \cdot (\mathcal{F} \dot{\mathbf{w}}) = \frac{\partial}{\partial z} (\mathcal{F} \dot{z}) + \frac{\partial}{\partial v_z} (\mathcal{F} \dot{v}_z) + \frac{\partial}{\partial Y} (\mathcal{F} \dot{Y}) \quad (13)$$

$$= \dot{z} \frac{\partial \mathcal{F}}{\partial z} + \dot{v}_z \frac{\partial \mathcal{F}}{\partial v_z} \quad (14)$$

where  $\frac{dY}{dt} = 0$  as the stellar labels are assumed to be time invariant. By expanding the derivatives in Equation 14, this expression simplifies to

$$\dot{z} \frac{\partial \mathcal{F}}{\partial z} + \dot{v}_z \frac{\partial \mathcal{F}}{\partial v_z} = p_y \left( \dot{z} \frac{\partial f}{\partial z} + \dot{v}_z \frac{\partial f}{\partial v_z} \right) + f \left( \dot{z} \frac{\partial p_Y}{\partial z} + \dot{v}_z \frac{\partial p_Y}{\partial v_z} \right) \quad (15)$$

$$0 = \dot{z} \frac{\partial p_Y}{\partial z} + \dot{v}_z \frac{\partial p_Y}{\partial v_z} \quad (16)$$

where the first term in the right-hand side of Equation 15 is set to zero by the definition of the CBE (Equation 11). If we multiply Equation 16 by  $Y$  and integrate over all  $Y$  — i.e. compute the first moment of  $p_Y$ ,  $\langle Y \rangle = \int dY Y p_Y$  — we get an expression in terms of the mean stellar label,

$$0 = \frac{\partial \langle Y \rangle}{\partial z} \dot{z} + \frac{\partial \langle Y \rangle}{\partial v_z} \dot{v}_z \quad (17)$$

Rearranging Equation 17, we can write the vertical acceleration  $a_z$  as

$$a_z = -v_z \frac{\partial \langle Y \rangle}{\partial z} \left( \frac{\partial \langle Y \rangle}{\partial v_z} \right)^{-1} \quad (18)$$

where the right hand side and partial derivatives are evaluated along a curve of constant  $\langle Y \rangle$ , and we have replaced  $\frac{dv_z}{dt} = a_z$ . This works for any  $Y$  moments of the eDF,  $\mathcal{M}_Y = \int dY M(Y) \mathcal{F}$ , where  $M(Y)$  is a function of  $Y$  that defines the moment of interest. For simplicity below, as with the expressions above, we only use  $M(Y) = Y$  so that we use the mean stellar label  $\langle Y \rangle$  as our moment of choice.

In the next section, we develop a method for inferring the vertical acceleration profile  $a_z(z)$  that uses this motivation. In particular, it does not assume a form for the potential and instead parametrizes the dependence of  $\langle Y \rangle$  on the vertical phase space coordinates, which is sufficient for inferring the acceleration (Equation 18).

### 3.2. A Flexible Model of Stellar Label Moments in Phase Space

In this section, we develop a method to fit the shapes of contours of constant stellar label moments in the vertical phase space of the Milky Way disk. An example of the type of data we would like to model is shown in the middle panel of Figure 1, which shows the mean [Mg/Fe] abundances of stars in bins of vertical phase-space coordinates for stars on near-circular orbits in the solar neighborhood. As we showed in the previous

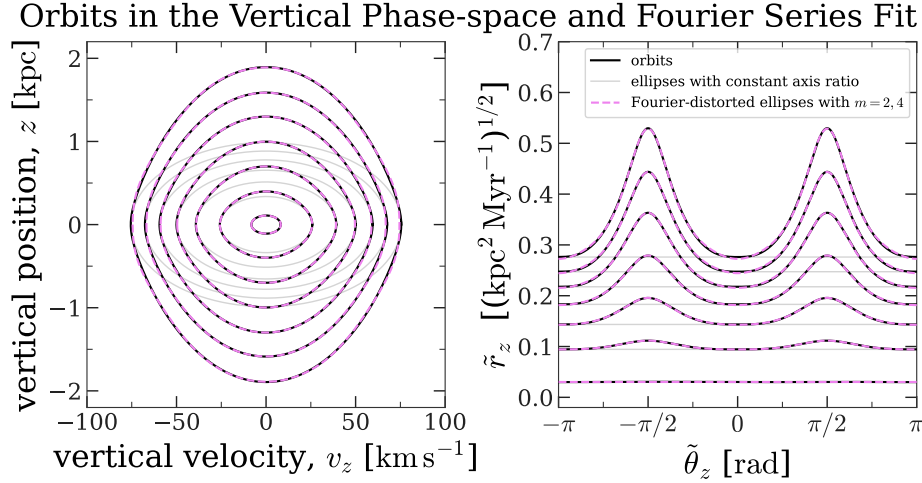


**Figure 2.** A demonstration that a low-order Fourier series expansion away from an ellipse can represent orbit shapes in the vertical phase space of the Milky Way disk. **Left panel:** The solid (black) lines show the same orbits as in Figure 1: These are seven orbits with equally-spaced values of the maximum height above the midplane each orbit reaches,  $z_{\max}$ , computed in a mass model for the Milky Way (see Appendix A). The dashed (pink) lines show a Fourier series expansion with  $m = \{2, 4\}$  with parameters  $(r_z, e_2, e_4)$  determined by fitting to each orbit. The under-plotted (gray) ellipses show ellipses with the same values of  $v_{z,\max}$  as the orbits to emphasize that the orbits have a changing axis ratio (i.e. frequency) with increased vertical action  $J_z$ . **Right panel:** The same orbits, Fourier series representations, and constant-frequency ellipses, but now shown in the elliptical radius,  $\tilde{r}_z$  (Equation 19) and angle,  $\tilde{\theta}_z$  (Equation 20).

section (Section 3.1), these contours of observed mean  $[\text{Mg}/\text{Fe}]$  abundance (or any moments of stellar labels) correspond to orbital trajectories, under the assumptions adopted above. To parametrize the shapes of the contours of constant stellar label, we use a Fourier expansion away from an elliptical radius in the vertical phase space, as described below.

As mentioned above (Section 2), orbits near the Galactic midplane ( $z \approx 0$ ) feel an approximately uniform mass density,  $\rho(z) \approx \rho_0$ . This implies that the vertical gravitational potential near the midplane will be close to a harmonic oscillator potential in which orbits have a constant vertical frequency  $\Omega_0$  (Equation 5). These orbits therefore trace closed ellipses of constant elliptical radius  $\tilde{r}_z$  defined as

$$\tilde{r}_z = \sqrt{z^2 \Omega_0 + v_z^2 \Omega_0^{-1}} \quad (19)$$

for all values of the corresponding elliptical angle  $\tilde{\theta}_z$ ,

$$\tan(\tilde{\theta}_z) = \left( \frac{z}{v_z} \right) \Omega_0 \quad . \quad (20)$$

For orbits near the midplane (i.e. with small  $J_z$ ),  $\tilde{r}_z \approx \sqrt{2 J_z}$ .

Away from the midplane, the shapes of orbits have steadily decreasing frequencies with increasing maximum height  $z_{\max}$ , which leads to, to first order, a changing aspect ratio of the contours. For example, the orbits in the left panels of Figure 1 and Figure 2 start as horizontal ellipses for the lowest values of  $z_{\max}$  and transition to vertical

ellipses for the largest values of  $z_{\max}$ . For contours with sufficiently large  $z_{\max}$  values (i.e. orbits that reach many scale heights above the disk), the decreasing density of the disk and the influence of the dark matter halo’s potential distorts the orbit shapes, and the contours of the DF are no longer well-approximated by ellipses (e.g., the orbits with  $z_{\max} \gtrsim 1$  kpc in Figure 2). Orbits with  $z_{\max} \gtrsim 1$  kpc deform from ellipses to more “diamond-like” shapes that are “pinched” near the midplane ( $z = 0$ ). This shape arises because the orbits feel a nearly uniform density at their vertical apocenter (i.e. near  $v_z = 0$ ), but then feel a rapidly changing potential as they cross the midplane (i.e. near  $z = 0$ ) with large vertical velocities.

To represent more general contour shapes (i.e. beyond ellipses), we use a low-order Fourier expansion in the elliptical angle  $\tilde{\theta}_z$  to distort the elliptical radius  $\tilde{r}_z$  (Equation 19) into the distorted elliptical radius  $r_z$ , defined as

$$r_z = \tilde{r}_z \left[ 1 + \sum_m \epsilon_m(\tilde{r}_z) \cos \left( m \tilde{\theta}_z \right) \right] \quad (21)$$

where, for the vertical kinematics, we only consider even  $m$  values to preserve the symmetry of the contour shapes. The functions  $\epsilon_m(\tilde{r}_z)$  describe the radius-dependent amplitude of the Fourier terms, which we require to be zero at  $\tilde{r}_z = 0$ , and the values are typically  $\ll 1$  for the orbits we consider (i.e. with  $z_{\max} \lesssim 2$  kpc or so). This expansion is motivated by the fact that we expect to need just a few Fourier terms: an  $m = 2$  distortion with an amplitude that varies with  $\tilde{r}_z$  will change the aspect ratio of the elliptical contours as a function of  $\tilde{r}_z$ , which acts like a changing frequency as a function of  $z_{\max}$ . An  $m = 4$  distortion can “pinch” the contour shapes to make them more diamond-like, which mimics the effect of an orbit feeling the halo potential. Figure 2 shows the same orbits as in the left panel of Figure 1 (solid black lines) along with a low-order Fourier expansion fit to these orbits (dashed pink lines), showing that even with just  $m = \{2, 4\}$  Fourier terms, we can accurately model the shapes of the orbits. The left panel of Figure 2 shows the orbits and Fourier fits in the vertical phase space, and the right panel shows the same orbits and Fourier fits in the elliptical radius and angle coordinates,  $\tilde{r}_z$  and  $\tilde{\theta}_z$ .

When fitting stellar label data, we assume that the contours of constant stellar label moments are only functions of the distorted radius,  $r_z$  (Equation 21). This then enforces that  $r_z$  is constant along a contour of constant label value and, therefore, nearly constant along a vertical orbit. We then need to specify a functional form for the dependence of the mean stellar label on  $r_z$ ,  $\langle Y \rangle(r_z)$ , which we assume is a smooth function of  $r_z$  but is otherwise customizable (we adopt choices below in the demonstrations in Section 4). The model components that must be specified in order to fit this model given a sample of stellar phase-space positions and labels are: the Fourier distortion amplitude functions  $\epsilon_m(\tilde{r}_z)$  for all  $m$  orders up to the specified  $M$ , the functional form and any parameters of the stellar label function  $\langle Y \rangle(r_z)$ , and the asymptotic midplane orbital frequency  $\Omega_0$ . As we will be fitting this model to data where we do not know the true zero-point position or velocity of the midplane, we

additionally include parameters  $z_0$  and  $v_{z,0}$  to represent these zero-point values — we then replace  $z$  and  $v_z$  in Equations 19–20 with  $z - z_0$  and  $v_z - v_{z,0}$ .

As the label function only depends on the distorted radius  $r_z$ , we can compute the vertical acceleration from a fitted OTI model directly from the dependence of  $r_z$  on the phase space coordinates. That is, from Equation 18 and applying the chain rule, we have

$$a_z = -v_z \frac{\partial r_z}{\partial z} \left( \frac{\partial r_z}{\partial v_z} \right)^{-1}. \quad (22)$$

From the definition of  $r_z$  and after some manipulation (see Appendix B), we find that

$$a_z(z) = -\Omega_0^2 z \frac{\left[ 1 + \sum_m^{2,\dots,M} (-1)^{m/2} \left( e_m(\tilde{r}_z) + \tilde{r}_z \frac{de_m}{d\tilde{r}_z} \right) \right]_{\tilde{r}_z=\sqrt{\Omega_0} z}}{\left[ 1 + \sum_m^{2,\dots,M} (-1)^{m/2} \left( e_m(\tilde{r}_z) (1 - m^2) + \tilde{r}_z \frac{de_m}{d\tilde{r}_z} \right) \right]_{\tilde{r}_z=\sqrt{\Omega_0} z}} \quad (23)$$

where  $M$  is the maximum (even) order of the Fourier expansion of the distorted radius, and the expression is evaluated at  $\tilde{r}_z = \sqrt{\Omega_0} z$ . Note that when  $e_m = 0$  for all  $m$  (i.e. when there is no distortion of the elliptical radius), this reduces to the expected expression for the simple harmonic oscillator.

We obtain the expression above for  $a_z(z)$  (Equation 23) by taking the limit  $\tilde{\theta}_z \rightarrow \pi/2$ , which, in our definition, is equivalent to the limit  $v_z \rightarrow 0$ . However, because our model parametrizes the shapes of orbits without imposing physicality, our inferred force law can end up depending on velocity. This is unphysical, but is a tradeoff we make to allow for a flexible model of the phase space — we discuss this point further in the Discussion (Section 5.1). Another potential pathology of our model setup is that, for some settings of the functions  $e_m(\tilde{r}_z)$ , the orbits can cross (i.e. the contours of constant label can intersect). In a truly separable system, this would also lead to unphysical interpretations of the force field inferred from the model, as the orbits should foliate the phase space. We do not find this to be a problem in practice with sufficient bounds set on the Fourier distortion functions to keep their amplitudes small.

We have implemented this new Orbital Torus Imaging (OTI) framework in *Python* using *JAX* (Bradbury et al. 2018) to accelerate the model evaluation and to use automatic differentiation to compute the gradients of the model with respect to the (many) model parameters. We release a software package, *torusimaging* (Price-Whelan 2024)<sup>2</sup>, along with this Article that contains our implementation. This framework is therefore very general and our implementation accepts any functional forms for the model components.

### 3.3. Computing empirical actions and angles

The distorted elliptical radius  $r_z$  will be close to constant along orbits in the vertical phase space. The orbital action and frequency should therefore be monotonic and smooth functions of  $r_z$ , i.e.  $J_z = J_z(r_z)$  and  $\Omega_z = \Omega_z(r_z)$ . We can therefore use a fitted model of the contours of constant stellar label to compute empirical values of the

<sup>2</sup> <https://github.com/adrn/torusimaging>

action, conjugate angle, and frequency for a given phase-space position  $(z, v_z)^*$ . We compute these dynamical quantities using the integrals in Equations 6–7 by integrating over the elliptical angle  $\tilde{\theta}_z$  along a contour of constant  $r_z$ :

$$J_z = \frac{2}{\pi} \int_0^{\pi/2} d\tilde{\theta}_z v_z(\tilde{\theta}_z) \left| \frac{dz}{d\tilde{\theta}_z} \right| \quad (24)$$

$$T_z = 4 \int_0^{\pi/2} \frac{d\tilde{\theta}_z}{v_z(\tilde{\theta}_z)} \left| \frac{dz}{d\tilde{\theta}_z} \right| \quad (25)$$

where the function  $v_z(\tilde{\theta}_z)$  and the Jacobian term  $\left| \frac{dz}{d\tilde{\theta}_z} \right|$  are evaluated along a curve of constant  $r_z$  corresponding to the phase-space coordinates  $(z, v_z)^*$ . The conjugate angle variable,  $\theta_z$ , is computed as the fractional time

$$\theta_z = \frac{2\pi}{T_z} \int_0^{\tilde{\theta}_z^*} \frac{d\tilde{\theta}_z}{v_z(\tilde{\theta}_z)} \left| \frac{dz}{d\tilde{\theta}_z} \right| \quad (26)$$

where  $\tilde{\theta}_z^*$  is the value of  $\tilde{\theta}_z$  corresponding to the phase-space coordinates  $(z, v_z)^*$ .

#### 4. APPLICATIONS TO SIMULATED DATA

In this section, we demonstrate the OTI framework described above using a set of simulated datasets of increasing complexity. We start by using a one-dimensional simple harmonic oscillator potential (Section 4.1), then use a more realistic multi-component (3D) galaxy model (Section 4.2–4.3), and finally use the final snapshot from an  $N$ -body simulation of a disk galaxy perturbed by an orbiting satellite (Section 4.4).

Each demonstration below follows the same general procedure: (1) We bin the data into pixels of the vertical phase space  $(z-v_z)$  and compute the mean element abundance in each pixel, (2) we fit the OTI model to the binned data and then use a Markov Chain Monte Carlo (MCMC) sampler to sample the posterior distribution of the model parameters, and (3) we compute the vertical acceleration profile and other dynamical quantities from the fitted and sampled models. Note that, as input to OTI, we bin the data into pixels of vertical position  $z$  and velocity  $v_z$  and compute the mean abundance value in each pixel, but we do not simulate uncertainties on the phase-space coordinates. This is not a requirement of OTI: We could also use the individual particle positions and simultaneously handle the uncertainties on the phase-space coordinates by parameterizing the full distribution  $p_Y(Y | z, v_z)$  (Equation 16). However, we have found that near the solar neighborhood with modern *Gaia* data, the uncertainty on the vertical position and velocity is typically comparable to our adopted pixel size, so we bin the data and work with moments of  $p_Y$  to speed up the evaluation of the likelihood. In the example cases below, we set the maximum bin edge in each coordinate as three times the 90th percentile value of the distributions of  $z$  and  $v_z$  for each simulated sample, and use 151 bins for each coordinate. These choices are arbitrary, but we have verified that the results are not sensitive to reasonable changes of these values. In the following subsections, we demonstrate that OTI can recover the true vertical acceleration profiles and other dynamical quantities for these simulated data sets.

#### 4.1. Simple Harmonic Oscillator

As an initial application, we simulate phase-space data in a harmonic oscillator potential,

$$\Phi_z(z) = \frac{1}{2} \omega^2 z^2 \quad (27)$$

by sampling from an isothermal distribution function<sup>3</sup>

$$p_z(J_z) = \frac{1}{s_z} e^{-\frac{J_z}{s_z}} \quad ; \quad J_z \in [0, \infty) \quad (28)$$

$$s_z = \sigma_{v_z}^2 / \omega \quad (29)$$

$$z = \sqrt{\frac{2J_z}{\omega}} \sin \theta_z \quad ; \quad v_z = \sqrt{2J_z \omega} \cos \theta_z \quad (30)$$

We adopt  $\omega = 0.08 \text{ rad Myr}^{-1}$  and  $\sigma_{v_z} = 50 \text{ km s}^{-1}$  as somewhat arbitrary choices meant to approximately match the observed vertical kinematics of stars near the solar position in the Galactic disk. We sample  $N = 2^{18} = 262\,144$  phase-space positions to use as our simulated data set, but we note that the precision of our measurements (especially at high  $z$ ) will depend on the sample size. We then assign each star a simulated element abundance value to serve as a stellar label  $Y$ : We use the relation between  $[\text{Mg}/\text{Fe}]$  and  $z_{\text{max}}$  from the APOGEE data (see the right panel of Figure 1) to assign each star a simulated value of  $Y_{[\text{Mg}/\text{Fe}]}$  by drawing from a Gaussian centered on the mean value from the linear relation with a standard deviation of 0.05 dex. That is, our simulated abundance values are drawn from

$$Y_{[\text{Mg}/\text{Fe}]} \sim \mathcal{N}(0.064 z_{\text{max}} + 0.009, 0.05) \quad (31)$$

where  $\mathcal{N}(\mu, \sigma)$  is a normal distribution with mean  $\mu$  and standard deviation  $\sigma$ . We then additionally simulate measurement errors on the abundance values by drawing an abundance uncertainty,  $\sigma_Y$ , for each star particle such that  $\log \sigma_Y \sim \mathcal{U}(-4, 0.5)$ , where  $\log$  is the natural logarithm and  $\mathcal{U}(a, b)$  is the uniform distribution over the domain  $[a, b]$ . Figure 3 (middle left panel) shows the mean simulated  $[\text{Mg}/\text{Fe}]$  abundance for stars in bins of vertical phase-space coordinates with the same color scale as in the middle panel of Figure 1 (i.e. the real APOGEE data).

We then fit the simulated mean abundance data in pixels of phase-space coordinates,  $\langle Y_{[\text{Mg}/\text{Fe}]} \rangle$ , using the OTI framework described above (Section 3). For this initial test case, we include only an  $m = 2$  term in our Fourier distortion of the elliptical radius (Equation 21). Our input data are the mean label values in each pixel  $j$  computed as

$$\langle Y_{[\text{Mg}/\text{Fe}]} \rangle_j = \frac{\sum_n^{N_j} \frac{Y_n}{\sigma_{Y,n}^2}}{\sum_n^{N_j} \frac{1}{\sigma_{Y,n}^2}} \quad (32)$$

where  $Y_n$  and  $\sigma_{Y,n}$  are the individual stellar abundance measurements and their uncertainties for the  $N_j$  stars (indexed by  $n$ ) within a given pixel  $j$ . To represent this

<sup>3</sup> We will use  $f(\cdot)$  to represent a distribution function, DF, that integrates to a number of stars, and  $p(\cdot)$  to represent any normalized probability distribution function (i.e. a DF that integrates to 1).

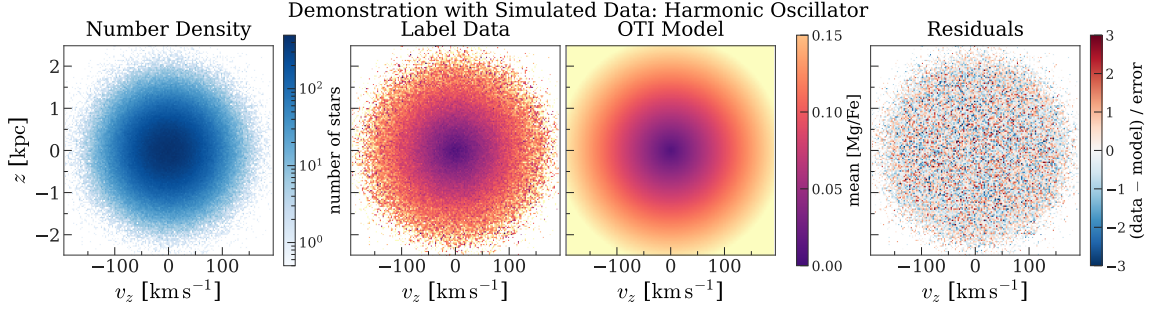


**Figure 3.** A demonstration of an optimized OTI model using simulated data in a simple harmonic oscillator potential. **Leftmost panel:** The number density of star particles for a simulated kinematic dataset in the vertical phase space using an isothermal distribution function embedded in a harmonic oscillator potential. **Middle left panel:** The same simulated vertical kinematics now showing the mean simulated  $[\text{Mg}/\text{Fe}]$  abundance values, generated assuming a linear relation between the mean  $[\text{Mg}/\text{Fe}]$  and  $z_{\text{max}}$  (see Figure 1). **Middle right panel:** The optimized OTI model evaluated on the same grid of phase-space coordinates as the data (middle left panel). **Rightmost panel:** The residuals of the optimized model normalized by the uncertainty in each pixel (i.e. the simulated data minus the optimized model, evaluated on the same grid of phase-space coordinates, and normalized). The small and uniform residuals show that the model accurately represents the mean abundance trends in this phase space.

data, we must decide on functional forms for both the label function,  $Y(r_z)$ , which will serve as our model prediction for the mean abundance in each pixel, and for the Fourier coefficient functions,  $e_m(\tilde{r}_z)$ , which here is just  $e_2(\tilde{r}_z)$ . For both of these functions,  $Y(r_z)$  and  $e_2(\tilde{r}_z)$ , we use monotonic quadratic spline functions defined such that the function is always monotonically increasing or decreasing, which must be set before optimization.

For the label function,  $Y(r_z)$ , we assert that the value must monotonically increase from  $r_z = 0$  to the maximum spline knot location by noting that the element abundance gradient has a positive slope from small values of the phase-space coordinates  $(z, v_z) \sim (0, 0)$  to larger values (see the middle left panel of Figure 3). We use  $K_Y = 8$  spline knot locations  $x_k^{(Y)}$  equally spaced in  $r_z$  between 0 and  $r_{z,\text{max}} \approx 0.7 \text{ kpc Myr}^{-0.5}$  with function values at the knot locations  $y_k^{(Y)}$ . This choice is arbitrary: We could here do a form of cross-validation to set the number of spline knots, but we set the number for simplicity.

For the Fourier coefficient function,  $e_2(\tilde{r}_z)$ , we require that the coefficient value must equal zero at  $\tilde{r}_z = 0$  (i.e.  $e_2(0) = 0$ ), and that the coefficient value monotonically increases with  $\tilde{r}_z$ . Requiring  $e_2(0) = 0$  ensures that the parameter  $\Omega_0$  corresponds to the asymptotic orbital frequency as  $\tilde{r}_z \rightarrow 0$  and can therefore be used to estimate the midplane volume mass density (Equation 5). Assuming that the coefficient value increases with  $\tilde{r}_z$  (so that the orbit shapes can only become more vertically stretched with increasing  $z_{\text{max}}$ ) is equivalent to assuming that the surface density increases with increasing height  $z$ . We use  $K_{e_2} = 8$  spline knot locations  $x_k^{(e_2)}$  with values  $y_k^{(e_2)}$  equally spaced in  $r_z^2$  between 0 and  $r_{z,\text{max}}$ , but we require the knot value at  $\tilde{r}_z = 0$  to be equal

to zero  $y_0^{(e_2)} = 0$ . When optimizing, we reparameterize to use  $\log \Omega_0$  and  $\log y_k$  for any spline coefficients as a trick to control the sign of the parameter values.

Our framework is implemented with JAX so that our objective function is just-in-time compiled and we can use automatic differentiation to compute the gradients of the objective function with respect to the, in this case, 18 model parameters: 8 spline knots for the label function, 7 spline knots for the  $e_2$  function (there are 8 knots, but the value at zero is fixed to zero, so only 7 free values), 2 parameters for centering  $z_0$  and  $v_{z,0}$ , and the asymptotic midplane frequency  $\Omega_0$ . We use a Gaussian log-likelihood for the mean [Mg/Fe] abundance data in each pixel of phase space. That is, the log likelihood of the data,  $\ln \mathcal{L}$ , is computed as

$$\ln \mathcal{L} = \sum_j \ln \mathcal{N}(\langle Y_{[\text{Mg/Fe}]} \rangle_j | Y_j, \sigma_{Y,j}) \quad (33)$$

where the sum is done over the  $j$  pixels,  $\langle Y_{[\text{Mg/Fe}]} \rangle_j$  is the mean abundance value in pixel  $j$  (computed as described above; Equation 32),  $Y_j$  is the model predicted mean abundance value in pixel  $j$ , and  $\sigma_{Y,j}$  is the uncertainty on the mean abundance. For the uncertainty on the mean abundance in each pixel  $\sigma_{Y,j}$ , we consider both the error on the mean (given heteroskedastic measurement errors on the abundances of each star particle,  $\sigma_{Y,i}$ ),

$$\sigma_{\mu_Y} = \sqrt{\frac{1}{\sum_i \frac{1}{\sigma_{Y,i}^2}}} \quad (34)$$

and the intrinsic scatter of abundances in each pixel. We assume for this case that we do not know the true intrinsic scatter that we simulated with in order to emulate working with real data, so we compute the error-deconvolved intrinsic scatter,  $s_y$ , of abundance values in the ten pixels with the most number of star particles. We take the uncertainty of the mean abundance  $\mu_{Y,j}$  in each pixel  $j$  to be

$$\sigma_{\mu_{Y,j}} = \sqrt{\sigma_{\mu_{Y,j}}^2 + s_Y^2/N_j} \quad (35)$$

where  $N_j$  is the number of star particles in pixel  $j$  and  $\sigma_{\mu_{Y,j}}$  is the error on the mean in the same pixel.

As a way to enforce smoothness of the spline functions, we use a Gaussian prior on the spline function derivatives evaluated at the knot locations with a standard deviation of 0.5 for the label function derivatives, and 0.2 for the Fourier coefficient function derivatives. We then optimize the model parameters using the sum of the log likelihood and the log prior to find the maximum a posteriori (MAP) model parameters, then use this to initialize a Markov Chain Monte Carlo (MCMC) sampling of the parameters, to assess uncertainty on the model parameters.

We use a standard L-BFGS-B optimizer (Byrd et al. 1995) to minimize the regularized negative log-probability as implemented in JAXopt (Blondel et al. 2021). For this simulated data set, the optimization runs in  $\sim 10$  s on a single CPU. The middle right panel of Figure 3 shows the MAP model evaluated over the domain of our simulated data in the left panel, and the right panel shows the residuals. The residuals everywhere indicate that the best-fit model matches the data well.

We use the optimized parameter values to initialize two MCMC chains using the Hamiltonian Monte Carlo “No U-turn Sampler” (NUTS) implemented in the `blackjax` (Cabezas et al. 2023) Python package. We run the chains for 1000 initial steps to allow the NUTS sampler to tune the hyperparameters of the sampling procedure (e.g., the mass matrix), and then run for an additional 1000 steps. The left panel of Figure 4 shows the maximum a posteriori (MAP) vertical acceleration profile,  $a_z(z)$  (computed with Equation 23), as the under-plotted black line, and the over-plotted, dashed (green) line shows the true vertical acceleration relation,  $a_z = -\omega^2 z$ . This demonstrates that, for this toy dataset, we are able to recover the true acceleration profile using OTI. In the same panel, we also plot a shaded (gray) polygon to represent the acceleration profile span for the 16th–84th percentile values of the MCMC samples. However, in this case, the uncertainty region is comparable to the thickness of the black line.

The middle panel of Figure 4 shows eight orbits with equally-spaced (but arbitrary) values of the vertical velocity at  $z = 0$ : The under-plotted solid (black) lines show the orbital trajectories inferred using the MAP parameter values with our OTI model, and the over-plotted dashed (green) lines show the true orbital trajectories for this toy model, demonstrating agreement. The right panel of Figure 4 shows the true vertical action values for all simulated particles on the vertical axis (i.e. the samples from the DF used to create the mean abundance data shown in the middle left panel of Figure 3) and our estimates for the vertical action of each star particle as the black point markers, computed using the MAP parameter values. We compute the actions, frequencies, and angles using Equations 24–26 evaluated at the phase-space coordinates of each star particle. The acceleration error at  $z = 1$  kpc is  $< 1\%$  (in fractional error) and the median action error is  $< 0.5\%$  for this toy dataset.

For this demonstration, we do not have to define a global model for the gravitational potential or the DF. We are able to recover the vertical acceleration profile using a flexible model of the shapes of orbits as traced by the stellar labels. The advantage of using very flexible spline functions for the label function and Fourier distortion functions is that our model is able to fit the input data well while making fewer strong assumptions. However, the disadvantage is that the model is not constrained to be physical and can therefore end up with, e.g., a Fourier distortion function form that violates physicality in the sense that the implied density could be negative or change discontinuously. In the next section, we show how this performs for a more realistic (but still equilibrium) galaxy model.

#### 4.2. Axisymmetric Quasi-isothermal Disk

As a next application of the OTI framework, we use a more realistic galaxy model to sample 3D positions and velocities of star particles and show that OTI can still recover the vertical dynamics. We use a quasi-isothermal disk distribution function (DF; Binney 2012) with parameters derived from fitting Milky Way stellar data (we use the “thin disk” parameters from Table 3 of Sanders & Binney 2015). We implement this DF using the `Agama` package (Vasiliev 2019) and sample  $5 \times 10^8$  phase-space

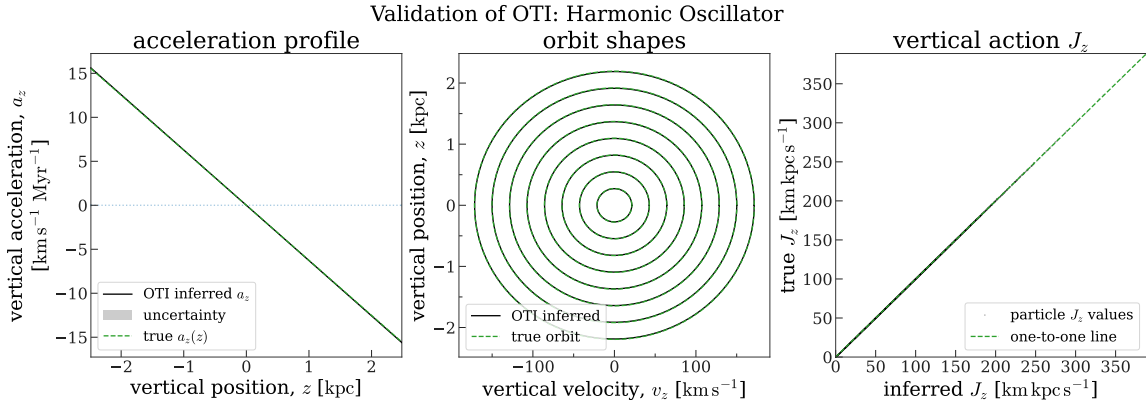


**Figure 4.** Validation of the OTI model fit to the simulated simple harmonic oscillator data. **Left panel:** The inferred (maximum a posteriori; MAP) vertical acceleration profile,  $a_z(z)$ , from the OTI model (solid black line) compared to the true acceleration profile (dashed green line). The uncertainty in the acceleration trend is comparable to the width of the line. Most of the simulated data are within  $|z| \lesssim 2$  kpc and the inferred acceleration profile agrees well with the true values within this region. **Middle panel:** Eight orbits with equally-spaced values of the vertical velocity computed in the true potential model (simple harmonic oscillator; shown as dashed, green lines) and with the OTI model using the MAP parameter values (solid, black lines). **Right panel:** A comparison of the true vertical action values (vertical axis) and our estimates using the MAP OTI model (horizontal axis). Our action estimates are empirical in that we do not need to assume the form for a gravitational potential. The median (fractional) action error is  $< 0.5\%$  for this sample dataset.

coordinates with guiding-center radii  $R_G$  between  $5 < R_G < 12$  kpc embedded in our adopted simple Milky Way potential model (see Appendix A). We compute the guiding radii using an approximation assuming the circular velocity curve,  $v_c(R)$ , is flat,  $R_G = L_z/v_c(R)$ , where  $L_z$  is the angular momentum of the star particle and  $R$  is its instantaneous cylindrical radius. From this simulated sample, we select only stars near the solar radius,  $R_0 = 8.3$  kpc, with  $|R - R_0| < 1$  kpc, and additionally select  $|R - R_G| < 1$  kpc and  $|v_R| < 15 \text{ km s}^{-1}$  as a way of limiting the radial action of the stars so that our assumption of  $R$ - $z$  separability is more valid. We do not use the radial action itself to select stars because we want to mimic the kinds of selections we could do with real data, where we do not know the true underlying gravitational potential (which would be needed to compute the actions). After these selections, we are left with  $\approx 7 \times 10^6$  star particles. We again compute simulated  $[\text{Mg}/\text{Fe}]$  abundance values for these stars using the linear relation between  $[\text{Mg}/\text{Fe}]$  and  $z_{\text{max}}$  from the APOGEE data (see the right panel of Figure 1) and a scatter of 0.05 dex (see Section 4.1), with simulated uncertainties again following the prescription outlined previously (Section 4.1). The left panels of Figure 5 shows this simulated data set in the vertical phase space coordinates.

We model the simulated mean abundance data in pixels of phase-space coordinates using the OTI framework described above (Section 3) and following the same procedure for optimizing and then MCMC sampling the model as in Section 4.1. We again use monotonic quadratic spline functions for both the label function and the Fourier coefficient functions. For the label function, we use 8 knots equally spaced in  $r_z$

between 0 and  $r_{z,\max} \approx 0.55 \text{ kpc Myr}^{-0.5}$ . However, here we use  $m = \{2, 4\}$  Fourier terms with 12 and 4 spline knots, respectively. We space the Fourier coefficient spline knots equally in  $r_z^2$  between 0 and  $r_{z,\max}$ . This places a higher density of knots at lower  $r_z$  values where we expect the Fourier coefficient functions to change more rapidly. We again require that the coefficient function values are zero at  $\tilde{r}_z = 0$  so that  $e_2(0) = e_4(0) = 0$ , and we assume that the overall sign of the functions are  $(+, -)$  for the  $m = \{2, 4\}$  coefficient functions, respectively.

We use the same priors as in Section 4.1 to lightly enforce smoothness of the derivatives of the spline functions. As above, we initially use a L-BFGS-B optimizer to minimize the regularized negative log-probability. This model has 22 parameters and optimizes in  $\sim 30$  seconds on a single CPU. The middle right panel of Figure 5 shows the best-fit model evaluated on the same pixel grid as the simulated data, and the rightmost panel shows the residuals between the optimized model and the data, normalized by the uncertainty on the mean abundance in each pixel. The small residuals indicate that this model does well to fit the mean abundance variations in the vertical phase space.

We again use the optimized parameter values to initialize an MCMC sampling of the parameters following the same procedure as in Section 4.1. The left panel of Figure 6 shows the inferred vertical acceleration profile (black line; computed with the MAP parameter values) and uncertainties (gray shaded region; computed using the 16th–84th percentile parameter values using the MCMC samples) along with the true vertical acceleration (green dashed line) evaluated at a constant  $R = R_0$  in our adopted Milky Way potential model (see Appendix A). The acceleration precision at  $z = 1 \text{ kpc}$  is  $\sim 1\%$  (in fractional error) with a  $\sim 1\%$  bias.

The middle panel of Figure 6 shows eight orbits with equally-spaced (but arbitrary) values of the vertical velocity at  $z = 0$ : The under-plotted solid (black) lines show the orbital trajectories inferred using the MAP parameter values with our OTI model, and the over-plotted dashed (green) lines show the true orbital trajectories. The true orbital trajectories are computed in the 3D galaxy model using the grid of  $v_z$  values at  $z = 0$  with  $x = R_0$ ,  $v_x = 0$ , and  $y = 0$ . To set  $v_y$  for the true orbits, we take the true actions computed for the particles in our selected region and fit a 3rd-order polynomial to the relationship between  $J_\phi$  and  $J_z$  in this region (which arises primarily because of the finite selection on  $R$ ). For the grid of  $v_z$  values, we transform to  $J_z$  and evaluate the fitted polynomial to obtain a  $J_\phi$  value, which we then convert to  $v_y$  by dividing out the radius  $R_0$ . There is good agreement between the true and inferred acceleration profile and orbits, especially for  $|z| \lesssim 1 \text{ kpc}$ . Above  $|z| \gtrsim 1 \text{ kpc}$ , the true orbit shapes and the OTI-inferred orbits begin to defer as the assumption of  $R$ – $z$  separability becomes less and less applicable.

We again compute the actions, frequencies, and angles for the star particles using Equations 24–26 evaluated at the phase-space coordinates of star particles in this simulated data set. The right panel of Figure 6 shows (as black markers) the true vertical action values for a random subset of  $10^5$  simulated particles on the vertical axis and our estimates for the vertical action of each star particle using the OTI model

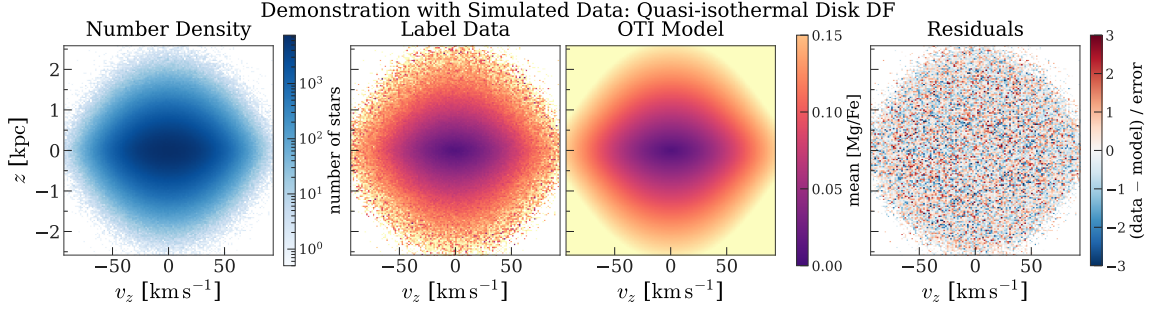


**Figure 5.** The same as Figure 3, but for the simulated quasi-isothermal disk sample from Section 4.2, showing the simulated data set (left and middle left panels), the optimized OTI model (middle panel), and the residuals (right panel).

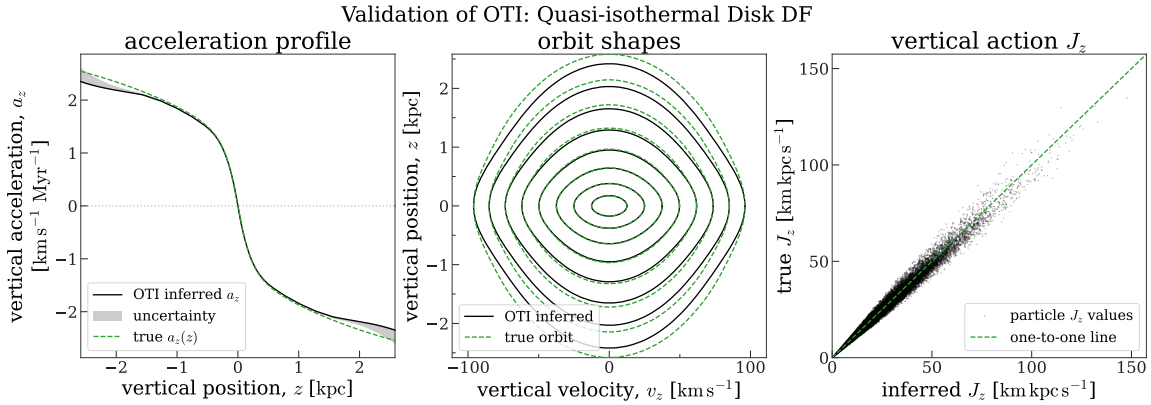


**Figure 6.** Validation of the OTI model fit to the simulated quasi-isothermal disk sample (i.e. the same as Figure 4, but for the simulated disk sample from Section 4.2). The median (fractional) action error is  $\approx 6\%$  for this sample dataset, but we do not need to assume a gravitational potential to compute the actions.

on the horizontal axis. We find the median fractional error of the vertical action, angle, and frequency are  $\sim 5\%$ ,  $\sim 6\%$ , and  $\sim 10\%$ , respectively. But again, we do not need to assume a gravitational potential to compute the values.

#### 4.3. Axisymmetric Quasi-isothermal Disk with Survey Selection

Real data from stellar surveys often has complex selection effects resulting from survey targeting and design, instrument limitations (e.g., magnitude limits), and/or real astronomical effects like bright stars, crowding, or dust extinction. All of these predominantly depend on position and brightness of the sources considered and not strongly on derived parameters like element abundances. One of the benefits of OTI is that positional selection effects do not bias our inferences so long as there are no strong correlations between the effective selection functions in position and the stellar labels considered. Here we demonstrate this by repeating the experiment in Section 4.2, but now after applying a  $z$ -dependent selection function such that the probability a source with a given  $z$  value appears in our dataset  $S(z)$  scales with

$$S(z) \propto \left( \frac{|z| + 150 \text{ pc}}{2 \text{ kpc}} \right)^2. \quad (36)$$

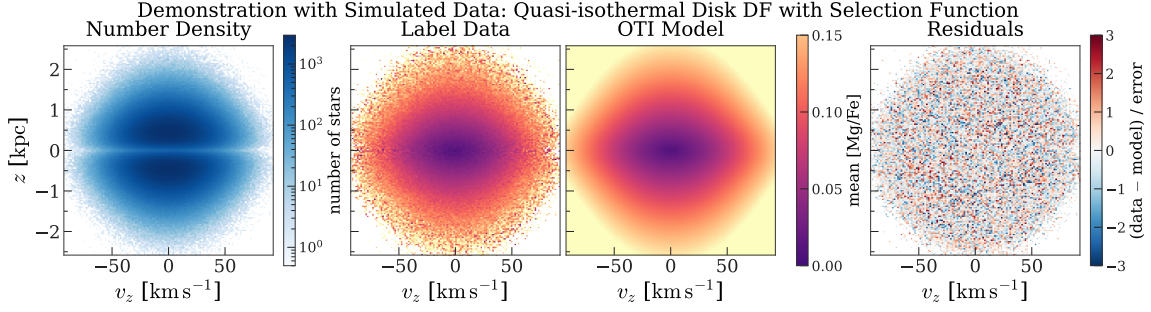


**Figure 7.** The same as Figure 3, but for the simulated quasi-isothermal disk sample with an imposed selection function that depends on  $z$  from Section 4.2. The left two panels show the simulated data set, the middle right panel shows the optimized OTI model, and the rightmost panel shows the residuals.

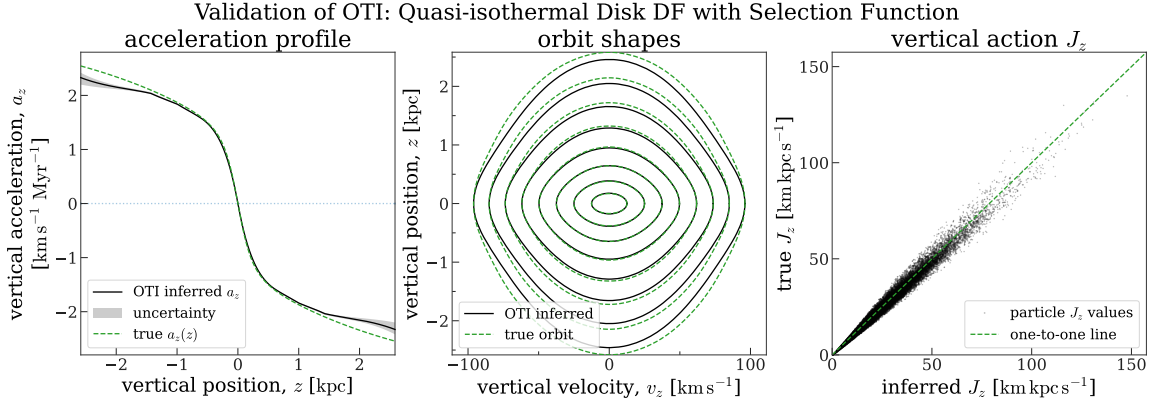


**Figure 8.** Validation of the OTI model fit to the simulated quasi-isothermal disk sample with an imposed selection function (i.e. the same as Figure 4, but for the simulated disk sample from Section 4.3). The model residuals in Figure 7 look reasonable, but this model has an unphysical gradient of the vertical acceleration (which would lead to negative density).

Figure 7 again shows the input data, where the left two panels show the number counts of stars per pixel of vertical phase-space coordinates and the mean (simulated)  $[\text{Mg}/\text{Fe}]$  abundance per pixel. The missing and lower density of stars near the midplane (mainly visible in the leftmost panel, relative to Figure 5) is the effect of our simulated selection function. The middle right panel again shows the OTI model evaluated at the MAP parameters after MCMC sampling, and the rightmost panel shows the residuals between the data and the MAP model. Even with the strong selection function, the OTI model leverages the strong (assumed) symmetries in the phase space to infer the orbit shapes even when data are missing. Figure 8 shows the validation of the OTI model fit to the data with a positional selection function imposed, demonstrating that the OTI model is still able to recover the true vertical acceleration profile and orbital shapes where our assumption of  $R$ - $z$  separability is most valid ( $|z| \lesssim 1$  kpc).

#### 4.4. *N-body Simulation with a Perturbed Disk*

As a final demonstration with simulated data, we apply the OTI framework to a section of an  $N$ -body simulation of a stellar disk that has been perturbed by an orbiting satellite galaxy. For this, we use the  $N$ -body simulation M1 of the **SMUDGE** simulation suite (Hunt et al. 2021) now available on **SciServer**<sup>4</sup> (Taghizadeh-Popp et al. 2020). M1 simulates the merger of a  $\sim 8 \times 10^{10} M_\odot$  dwarf galaxy consisting of two Hernquist spheres (Hernquist 1990) into a  $\sim 6 \times 10^{11} M_\odot$  disk galaxy host. The host galaxy consists of a  $8.8 \times 10^8$  particle live NFW halo (Navarro et al. 1997), a  $2.2 \times 10^7$  particle Hernquist bulge and a  $2.2 \times 10^8$  particle exponential disk with a high Toomre parameter  $Q = 2.2$  (Toomre 1964), following model MWb from Widrow & Dubinski (2005). For full details of the initial condition and simulation setup see Hunt et al. (2021).

The merger simulation is evolved for  $\sim 8.3$  Gyr using the GPU-based  $N$ -body tree code **Bonsai** (Bédorf et al. 2012, 2014). Following Hunt et al. (2021) we choose snapshot 702 (occurring at  $t = 6.874$ ) as the ‘present day’ snapshot used in this work, as this is the snapshot where satellite is closest to the location of the Sagittarius dwarf galaxy in the Milky Way. However, we stress that model M1 is not meant to reproduce the Milky Way–Sagittarius interaction (for which the reader should see Bennett et al. 2022) but instead be a laboratory for exploring satellite induced perturbation in an otherwise stable disk. We use a snapshot of the simulation after four pericentric passages, and six disk crossings of the satellite (see Figure 3 of Hunt et al. 2021, for the orbit and mass loss of the satellite), which induces significant non-axisymmetric kinematic structure in the disk. This application is a test of how well OTI can do (i.e. how biased the results are) in the presence of strong disequilibrium, which violates the assumptions laid out above.

We select a small region of the disk near the solar radius,  $R = 8$  kpc, by selecting all star particles within  $|x - -\text{kpc}| < 1$  kpc and  $|y| < 1$  kpc. We again mimic dynamical selections we could perform on real data by selecting stars near their guiding-center radius  $R_G$ , i.e.  $|R - R_G| < 1$  kpc, and with small radial velocity  $|v_R| < 15 \text{ km s}^{-1}$ . These dynamical selections limit the radial action of the stars so that our assumption of  $R$ – $z$  separability is less invalid, but does not require computing actions for the star particles before selection. We compute the guiding radii using the circular velocity curve of the simulated disk,  $R_G \approx L_z/v_c(R)$ , but here we use actions only to select a sample of stars on nearly circular orbits with which to measure the circular velocity. We compute the circular velocity by selecting star particles with low radial and vertical action (below the 15th percentile values of the radial and vertical actions, respectively) and compute the mean azimuthal velocity  $\langle v_\phi(R) \rangle$  as a function of cylindrical radius  $R$ , then adopt  $v_c(R) = \langle v_\phi(R) \rangle$ .

The “true” comparison actions are computed using **Agama** (Vasiliev 2019). We first approximate the host galaxy potential using two multipole expansions for the stellar bulge and dark matter halo, and an axisymmetric **CylSpline** expansion for the disk. We calculate actions, angles, and frequencies in the reconstructed potential

<sup>4</sup> <https://sciserver.org/datasets/smudge/>

using Agama’s `ActionFinder`. We note that, in this case, there is no ground truth for the actions, as the galaxy potential model is only approximate and any method for computing actions will have some additional approximation error.

We use these orbital actions to “paint” element abundances onto star particles in this idealized  $N$ -body simulation without gas or star formation. We compute the actions at an early snapshot of the simulation, after relaxation of the initial conditions and before the first pericentric passage of the satellite galaxy. We use the vertical actions of the star particles at this early snapshot to assign a simulated  $[\text{Mg}/\text{Fe}]$  abundance value to each star particle following the procedure explained in Section 4.2. We then track the abundance values through to the final snapshot where the actions have evolved due to satellite perturbations. To better emphasize the disequilibrium in the space of abundances, we reduce the intrinsic scatter of the abundances relative to the value estimated from APOGEE data (Figure 1) to be 0.05/4 instead of 0.05.

The left two panels of Figure 9 show the number density of stars in this volume, and the mean simulated  $[\text{Mg}/\text{Fe}]$  abundance of star particles in the vertical phase space of the “solar neighborhood” of the simulated stellar disk. While the overall pattern is similar to the smooth examples (e.g., Section 4.2), the mean abundance values here show appreciable asymmetries due to the perturbations from the simulated satellite galaxy. The middle right panel of Figure 9 shows the mean  $[\text{Mg}/\text{Fe}]$  of the optimized OTI model for this simulated data set, and the rightmost panel again shows the residuals. While the residuals are generally low, the residuals here have clear structure: There is a faint spiral pattern in the abundance residuals that is an analog to the vertical phase spiral seen in *Gaia* data in the number densities of stars. The presence of this abundance spiral in this simulated data should bias our inferred dynamical quantities.

Figure 10 (left panel) shows the vertical acceleration profile inferred by OTI for this region of the simulated disk (black line and gray shaded region) compared to the true acceleration profile (green dashed line). Within  $|z| \lesssim 0.5$  kpc, the OTI model agrees well with the true acceleration profile. However, for  $|z| \gtrsim 0.5$  kpc the OTI model clearly diverges from the truth with a bias at  $|z| = 1$  kpc of about 15%. The right panel of Figure 10 shows a comparison of vertical action values computed with the best-fit OTI model (horizontal axis) and with Agama (vertical axis). As mentioned above, the actions computed with Agama are not necessarily “true” values, as this system is not in equilibrium or symmetric, but the adopted potential model used to compute the actions is both axisymmetric and time-invariant. We find a median fractional difference of  $\sim 6\%$  for the vertical action values,  $\sim 12\%$  for the vertical frequencies, and  $\sim 5\%$  for the vertical angles. For real Milky Way stars, we expect similar biases due to the presence of the vertical phase spiral (Antoja et al. 2018).

## 5. DISCUSSION

In the subsections below, we return to our assumptions and several of the points raised in the results above to discuss the implications of our work and the limitations of the Orbital Torus Imaging (OTI) framework.

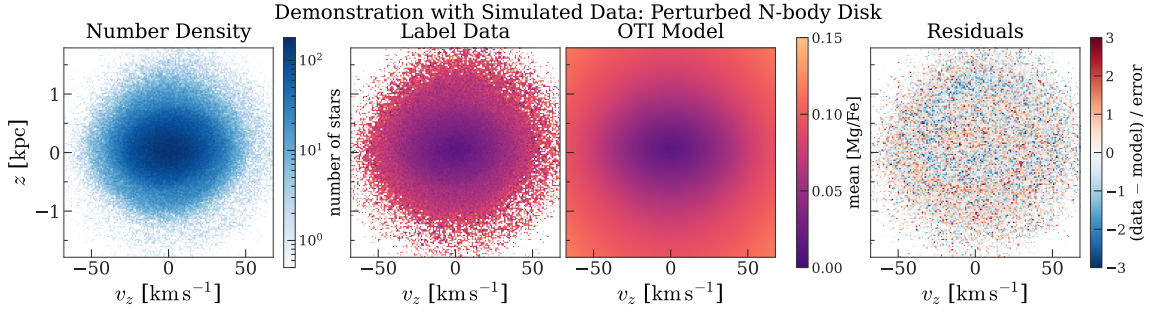


**Figure 9.** The same as Figure 3, but for data from a small region of a live  $N$ -body simulation of a disk galaxy perturbed by an orbiting satellite on an orbit similar to that predicted for the Sagittarius dwarf galaxy. The vertical structure of the simulated disk is perturbed repeatedly by interactions with the satellite, which create a vertical phase spiral in the number density of stars (leftmost panel) and weaker signatures of disequilibrium in simulated element abundances (middle left panel). The middle right panel again shows the optimized OTI model for these data, and the rightmost panel shows the (normalized) residuals.

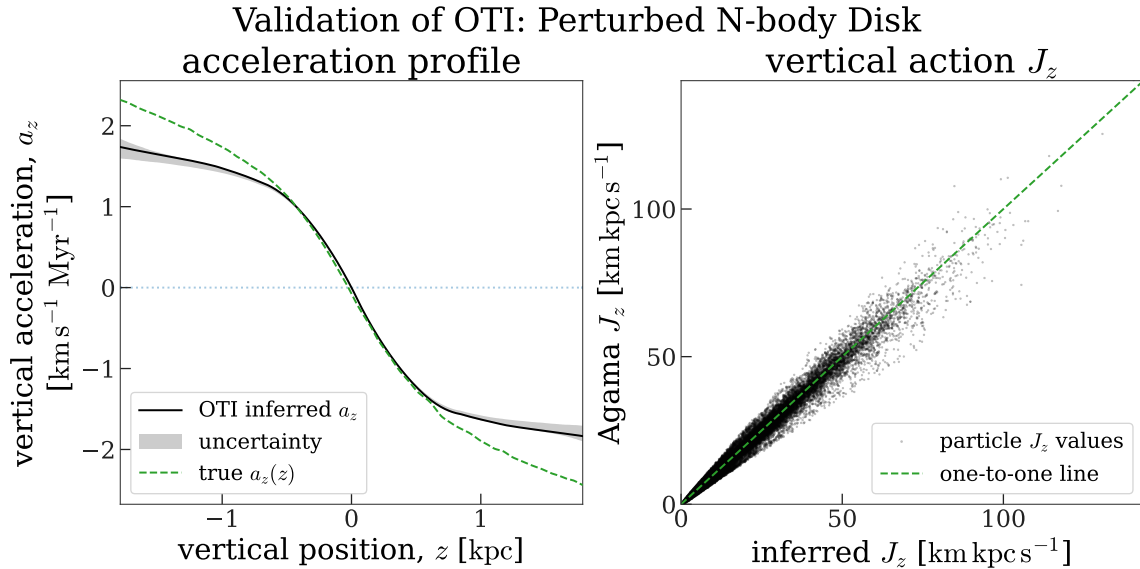


**Figure 10.** Validation of the OTI model fit to the vertical phase space of a small volume from an  $N$ -body simulation of a disk galaxy perturbed by an orbiting satellite. The left panel shows the inferred vertical acceleration profile and uncertainties (black line and gray shaded region) compared to the true acceleration profile (green dashed line). The inferred acceleration profile is biased for  $|z| \gtrsim 0.5$  kpc by the disequilibrium. The right panel shows a comparison of vertical action values computed with the best-fit OTI model (horizontal axis) and with Agama, using a time-independent reconstruction of the total gravitational potential of the simulated disk and dark matter halo (vertical axis).

### 5.1. The Tradeoff of Flexibility and Physicality

The OTI framework provides a flexible means for inferring the orbit structure and, therefore, the mass distribution underlying phase-mixed, tracer stellar populations. It works by parameterizing and modeling the shapes of contours of constant stellar labels in phase space. By assuming that these contours correspond to orbits, we can use the changing shapes of the contours to infer the underlying total gravitational

acceleration profile traced by the observed stars. In this way, it decouples the problem of modeling the phase space variation of stellar labels from the interpretation step, when this variation is mapped to the underlying gravitational field. It is flexible in that it does not require a global model for the gravitational potential or the DF, but instead uses the data itself to infer the orbit structure. However, this flexibility and this separation of modeling the phase space from physical interpretation can come at the cost of physicality.

Though it is possible to instantiate an OTI model with specific physical constraints (e.g., that the orbits follow a gravitational potential and the density is positive), the general OTI framework does not require this. As was shown with our demonstrations above (Section 4), this can lead to unphysical inferred acceleration profiles that arise both because of the presence of disequilibrium and because of the breakdown of our assumption of  $R$ - $z$  separability (Sections 4.3–4.4). What we gain from this flexibility is the ability to fit the phase space data very well, in ways that more constrained equilibrium models may find stronger residuals. Depending on the scientific goal, this may be a worthwhile tradeoff. For example, one may only want a flexible, symmetric model of the phase space to act as a filter to subtract and study the morphology of substructure (e.g., the *Gaia* phase spiral; Antoja et al. 2018). If one wants to infer the acceleration profile or other dynamical quantities (e.g., orbital actions, frequencies, or angles), the model must be validated by assessing the physicality of the inferred quantities. Or, one must use a more constrained model by adopting functional forms for the Fourier distortion functions and/or the label function that only permit physical solutions for the acceleration and density field. We leave this as a topic for future work.

## 5.2. *The Impact of Disequilibrium*

The Milky Way’s disk is now known to be out of equilibrium, especially in terms of the vertical kinematics of stars (e.g., Antoja et al. 2018; Gaia Collaboration et al. 2018; Ramos et al. 2018; Tian et al. 2018; Laporte et al. 2019; Khanna et al. 2019; Hunt et al. 2022; Darragh-Ford et al. 2023). The imprint of the vertical “phase spiral” is apparent in both the phase-space density in the Milky Way and even in the mean element abundances of stars (Frankel et al. in prep.). Non-phase-mixed structures in the vertical kinematics violate our assumptions and will generally bias our inferred orbit shapes and acceleration profile, as demonstrated in Section 4.4. In this work, we simply highlight this potential bias and do not attempt to correct for this in our demonstrations above. However, there is a path toward accounting for weak disequilibrium in the framework outlined above.

In the limit that the dependence of stellar label moments on the phase-space coordinates is a sum of a smooth, equilibrium component and a low-amplitude, phase-coherent component, we can build the phase-dependence of the stellar labels directly into the OTI model. In what we have done in this work, in terms of the vertical phase space, we have assumed that the stellar labels  $Y$  or moments of the stellar labels  $\langle Y \rangle$  only depend on the distorted elliptical radius  $r_z$  (Equation 21) such that, e.g.,

$Y = Y(r_z)$ . We can generalize this to allow for a phase-coherent component by instead making  $Y = Y(r_z, \theta_z)$ , where  $\theta_z$  is the vertical angle (Equation 26), which can be computed internally within the OTI model for a given setting of the parameters. We consider a full exploration of this extensions as out of scope for this work, but hope to explore this in the future.

### 5.3. *Beyond Vertical Dynamics*

While this work primarily focuses on the vertical dynamics of stars in the Milky Way disk, a natural extension of the current description of the OTI framework is to consider the radial  $R$  and azimuthal  $\phi$  dependencies as well. In principle, the OTI framework is applicable in any projection of phase space, meaning it is possible to extend the framework to model the dynamics in the entire 6D phase space. Incorporating the radial dependence of the stellar labels and their moments would allow us to connect and jointly model regions of the disk in a flexible framework that does not require imposing a global model of the potential or density distribution. As it is currently implemented, we can only achieve this by binning the data into regions of  $R$  and/or  $\phi$  to consider a single projection of the phase space. However, even within this model, we could explore instead the  $\Delta R = R - R_G$  vs.  $v_R$  phase space as a complementary view of the dynamics of the Milky Way disk. We hope to explore this in future work.

Another avenue for exploration is the possibility of going coordinate-free, or at least projection-free, to identify surfaces in the full 6D phase space upon which stellar label moments remain approximately constant. Under the assumptions described above, these surfaces would correspond to the orbital tori of stars and would allow us to directly map the Galaxy’s orbit structure. A first exploration of this more general path is considered in [Novara et al. \(in prep.\)](#).

### 5.4. *What stellar labels are useful for OTI?*

As mentioned above (Section 4.3), a critical requirement for OTI is that the selection function on stellar phase-space coordinates is separable from the selection function of the stellar labels considered (see Section 1). For element abundances, this is mostly true for surveys like APOGEE, where the primary survey target selection is done based on color and magnitude, which only weakly depend on surface abundances ([Zasowski et al. 2017](#); [Santana et al. 2021](#); [Beaton et al. 2021](#)). However, this also implies that stellar surface gravity,  $\log g$ , or effective temperature,  $T_{\text{eff}}$ , would *not* be useful stellar labels within the OTI framework because they are strongly covariant with luminosity or absolute magnitude. Additionally, there is a potential danger in using kinematic measurements that are inferred from spectroscopy (e.g., spectrophotometric distances; [Hogg et al. 2019](#); [Leung & Bovy 2019](#)) in OTI: If the kinematic measurements are inferred from the spectra, even if the target selection is separable, the estimators may inject correlations between the stellar labels and the phase-space coordinates.

The method presented here works for any moments of any stellar labels that satisfy the condition that the selection function on the stellar labels is separable from the selection function on the phase-space coordinates. Can we therefore combine the likelihoods from multiple element abundances or multiple moments of the abundances

to improve the precision of our inferences? In principle, yes, but element abundances tend to be strongly correlated with each other (e.g., [Ness et al. 2019](#); [Griffith et al. 2023](#)), so the different moments and/or abundances must be incorporated conditionally (e.g., [Ratcliffe & Ness 2023](#)). We will explore this in future work.

## 6. SUMMARY AND CONCLUSIONS

We introduce a new formulation and implementation of the Orbital Torus Imaging (OTI) framework. We derive a rigorous justification for OTI based on dynamical theory, and demonstrate its utility for inferring the orbital structure of stellar populations and characterizing the underlying gravitational field using stellar labels. OTI works by parameterizing and modeling the shapes of contours of constant stellar labels or constant moments of the stellar label distribution in regions of phase space. By assuming that these contours correspond to orbits, we use the changing shapes of the contours to infer the underlying total gravitational acceleration profile traced by the observed stars. OTI is less sensitive to selection effects than traditional methods that model the stellar phase-space density, and does not require specifying a global model for the gravitational potential or the stellar distribution function. We demonstrate the flexibility of OTI in modeling and recovering the true underlying gravitational field for simulated tracer stellar populations in toy and more realistic settings in the vertical phase space. However, the mathematical formulation of OTI applies to a wider range of systems, both with higher dimensions (e.g., axisymmetric systems) and out of equilibrium (e.g., with weak disequilibrium). The OTI framework is implemented in the open-source Python package `torusimaging` ([Price-Whelan 2024](#)). In our companion paper, we use the OTI framework to measure the vertical acceleration profile and the mass distribution of the Milky Way disk using APOGEE data ([Horta et al. 2023](#)). Future data releases from *Gaia*, SDSS-V, and upcoming spectroscopic surveys will enable new and more precise measurements of the Milky Way’s gravitational field using OTI.

1 It is a pleasure to thank Neige Frankel, Melissa Ness, Julianne Dalcanton, and the  
 2 *Nearby Universe Group* at the CCA for useful discussions and feedback on this work.

3 KJV’s contributions were supported by a grant from the Simons Foundation (CCA  
 4 1018465). LMW was supported by a Discovery Grant with the Natural Sciences and  
 5 and Engineering Research Council of Canada.

6 Funding for the Sloan Digital Sky Survey IV has been provided by the Alfred  
 7 P. Sloan Foundation, the U.S. Department of Energy Office of Science, and the  
 8 Participating Institutions. SDSS-IV acknowledges support and resources from the  
 9 Center for High-Performance Computing at the University of Utah. The SDSS web  
 10 site is [www.sdss.org](http://www.sdss.org).

11 SDSS-IV is managed by the Astrophysical Research Consortium for the Partici-  
 12 pating Institutions of the SDSS Collaboration including the Brazilian Participation  
 13 Group, the Carnegie Institution for Science, Carnegie Mellon University, the Chilean  
 14 Participation Group, the French Participation Group, Harvard-Smithsonian Center  
 15 for Astrophysics, Instituto de Astrofísica de Canarias, The Johns Hopkins University,  
 16 Kavli Institute for the Physics and Mathematics of the Universe (IPMU) / University  
 17 of Tokyo, Lawrence Berkeley National Laboratory, Leibniz Institut für Astrophysik  
 18 Potsdam (AIP), Max-Planck-Institut für Astronomie (MPIA Heidelberg), Max-Planck-  
 19 Institut für Astrophysik (MPA Garching), Max-Planck-Institut für Extraterrestrische  
 20 Physik (MPE), National Astronomical Observatories of China, New Mexico State  
 21 University, New York University, University of Notre Dame, Observatório Nacional /  
 22 MCTI, The Ohio State University, Pennsylvania State University, Shanghai Astro-  
 23 nomical Observatory, United Kingdom Participation Group, Universidad Nacional  
 24 Autónoma de México, University of Arizona, University of Colorado Boulder, Univer-  
 25 sity of Oxford, University of Portsmouth, University of Utah, University of Virginia,  
 26 University of Washington, University of Wisconsin, Vanderbilt University, and Yale  
 27 University.

28 This work has made use of data from the European Space Agency (ESA) mis-  
 29 sion *Gaia* (<https://www.cosmos.esa.int/gaia>), processed by the *Gaia* Data Process-  
 30 ing and Analysis Consortium (DPAC, [https://www.cosmos.esa.int/web/gaia/dpac/](https://www.cosmos.esa.int/web/gaia/dpac/consortium)  
 31 [consortium](https://www.cosmos.esa.int/web/gaia/dpac/consortium)). Funding for the DPAC has been provided by national institutions, in  
 32 particular the institutions participating in the *Gaia* Multilateral Agreement.

*Software:* Agama (Vasiliev 2019), Astropy (Astropy Collaboration et al. 2013,  
 2018, 2022), gala (Price-Whelan 2017), JAX (Bradbury et al. 2018), JAXOpt (Blondel  
 et al. 2021), matplotlib (Hunter 2007), numpy (Harris et al. 2020), pyia (Price-Whelan  
 2018), scipy (Virtanen et al. 2020), torusimaging (Price-Whelan 2024).

## APPENDIX

### A. A TOY MILKY WAY MASS MODEL

For the demonstrations with equilibrium models above (Section 4.2–4.3), we use a simplistic mass model to represent the total gravitational potential of the Milky Way. We use a two component model consisting of a Miyamoto–Nagai disk (Miyamoto & Nagai 1975) embedded in a spherical Navarro–Frenk–White (NFW) halo (Navarro et al. 1997). We adopt the following parameter values for the disk and halo, respectively:  $M_{\text{disk}} = 6.91 \times 10^{10} M_{\odot}$ ,  $a = 3$  kpc,  $b = 0.25$  kpc,  $M_{\text{halo}} = 5.4 \times 10^{11} M_{\odot}$ ,  $r_s = 15$  kpc, where  $a$  and  $b$  are the disk scale length and scale height, respectively,  $M_{\text{halo}}$  is the scale mass of the halo (not the virial mass), and  $r_s$  is the scale radius of the halo. These values are chosen so that the circular velocity at the solar radius  $R_0 = 8.3$  kpc is  $v_c(R_0) = 229 \text{ km s}^{-1}$ , and other parameters are chosen to be consistent with the MilkyWayPotential2022 implemented in `gala` (Price-Whelan 2017).

### B. EVALUATION OF THE VERTICAL ACCELERATION FROM AN OTI MODEL

We evaluate the vertical acceleration as a function of height above the Galactic midplane,  $a_z(z) = \frac{d\Phi}{dz}$ , given an OTI model and parameters using Equation 22, reproduced here:

$$a_z = -v_z \frac{\partial r_z}{\partial z} \left( \frac{\partial r_z}{\partial v_z} \right)^{-1} \quad (\text{B1})$$

The acceleration only depends on the shapes of the contours of the DF, i.e. curves of constant  $r_z$ , so that we only need to differentiate the distorted radius to evaluate it. Based on our definitions above (Equations 19, 21, and 26), the partial derivatives of  $r_z$  with respect to  $z$  and  $v_z$  are:

$$\frac{\partial r_z}{\partial z} = \frac{\partial \tilde{r}_z}{\partial z} + \sum_{m=2}^M \frac{\partial}{\partial z} \left[ \tilde{r}_z e_m(\tilde{r}_z) \cos(m \tilde{\theta}_z) \right] \quad (\text{B2})$$

$$\frac{\partial r_z}{\partial v_z} = \frac{\partial \tilde{r}_z}{\partial v_z} + \sum_{m=2}^M \frac{\partial}{\partial v_z} \left[ \tilde{r}_z e_m(\tilde{r}_z) \cos(m \tilde{\theta}_z) \right] \quad (\text{B3})$$

Plugging these in to Equation 22, and using the following expressions

$$\frac{\partial \tilde{r}_z}{\partial z} = \frac{z \Omega_0}{\tilde{r}_z} \quad ; \quad \frac{\partial \tilde{r}_z}{\partial v_z} = \frac{v_z}{\Omega_0 \tilde{r}_z} \quad (\text{B4})$$

$$\frac{\partial \tilde{\theta}_z}{\partial z} = \frac{v_z}{\tilde{r}_z^2} \quad ; \quad \frac{\partial \tilde{\theta}_z}{\partial v_z} = -\frac{z}{\tilde{r}_z^2} \quad (\text{B5})$$

$$\frac{\partial e_m}{\partial z} = \frac{\partial e_m}{\partial \tilde{r}_z} \frac{\partial \tilde{r}_z}{\partial z} \quad ; \quad \frac{\partial e_m}{\partial v_z} = \frac{\partial e_m}{\partial \tilde{r}_z} \frac{\partial \tilde{r}_z}{\partial v_z} \quad (\text{B6})$$

our goal is to remove or collect terms that explicitly contain  $v_z$ , as the acceleration should not depend on velocity (though we do not require this in the OTI framework).

With this in mind, and using the expressions listed above to simplify, we find that

$$\frac{\partial r_z}{\partial z} = \frac{\partial \tilde{r}_z}{\partial z} + \sum_{m=2}^M \frac{\partial}{\partial z} \left[ \tilde{r}_z e_m(\tilde{r}_z) \cos(m \tilde{\theta}_z) \right] \quad (\text{B7})$$

$$= \frac{z \Omega_0}{\tilde{r}_z} \left[ 1 + \sum_{m=2}^M \left( \left( e_m + \tilde{r}_z \frac{de_m}{d\tilde{r}_z} \right) \cos(m \tilde{\theta}_z) - m e_m \frac{\sin(m \tilde{\theta}_z)}{\sin(\tilde{\theta}_z)} \cos(\tilde{\theta}_z) \right) \right] \quad (\text{B8})$$

As we are interested in evaluating this expression along the  $z$ -axis, we will take the limit of this expression as  $\tilde{\theta}_z \rightarrow \frac{\pi}{2}$ , which is equivalent to the limit  $v_z \rightarrow 0$ . For even values of  $m$ , as we require, the sine term in the sum of Equation B8 will be zero, and the cosine terms become:

$$\cos(m \tilde{\theta}_z) = (-1)^{m/2} \quad . \quad (\text{B9})$$

In this limit, the expression becomes:

$$\lim_{\tilde{\theta}_z \rightarrow \frac{\pi}{2}} \frac{\partial r_z}{\partial z} = \frac{z \Omega_0}{\tilde{r}_z} \left[ 1 + \sum_{m=2}^M (-1)^{m/2} \left( e_m + \tilde{r}_z \frac{de_m}{d\tilde{r}_z} \right) \right] \quad . \quad (\text{B10})$$

Similarly for the derivative with respect to  $v_z$ :

$$\frac{\partial r_z}{\partial v_z} = \frac{\partial \tilde{r}_z}{\partial v_z} + \sum_{m=2}^M \frac{\partial}{\partial v_z} \left[ \tilde{r}_z e_m(\tilde{r}_z) \cos(m \tilde{\theta}_z) \right] \quad (\text{B11})$$

$$= \frac{v_z}{\Omega_0 \tilde{r}_z} \left[ 1 + \sum_{m=2}^M \left( \left( e_m + \tilde{r}_z \frac{de_m}{d\tilde{r}_z} \right) \cos(m \tilde{\theta}_z) + m e_m \sin(m \tilde{\theta}_z) \tan(\tilde{\theta}_z) \right) \right] \quad (\text{B12})$$

Taking the same limit  $\tilde{\theta}_z \rightarrow \frac{\pi}{2}$ , this expression becomes:

$$\lim_{\tilde{\theta}_z \rightarrow \frac{\pi}{2}} \frac{\partial r_z}{\partial v_z} = \frac{v_z}{\Omega_0 \tilde{r}_z} \left[ 1 + \sum_{m=2}^M (-1)^{m/2} \left( e_m (1 - m^2) + \tilde{r}_z \frac{de_m}{d\tilde{r}_z} \right) \right] \quad . \quad (\text{B13})$$

Combining these expressions, we have:

$$a_z = -v_z \frac{\partial r_z}{\partial z} \left( \frac{\partial r_z}{\partial v_z} \right)^{-1} \quad (\text{B14})$$

$$= -v_z \frac{z \Omega_0}{\tilde{r}_z} \frac{\Omega_0 \tilde{r}_z}{v_z} \frac{\left[ 1 + \sum_{m=2}^M (-1)^{m/2} \left( e_m + \tilde{r}_z \frac{de_m}{d\tilde{r}_z} \right) \right]}{\left[ 1 + \sum_{m=2}^M (-1)^{m/2} \left( e_m (1 - m^2) + \tilde{r}_z \frac{de_m}{d\tilde{r}_z} \right) \right]} \quad (\text{B15})$$

$$= -\Omega_0^2 z \frac{\left[ 1 + \sum_{m=2}^M (-1)^{m/2} \left( e_m + \tilde{r}_z \frac{de_m}{d\tilde{r}_z} \right) \right]}{\left[ 1 + \sum_{m=2}^M (-1)^{m/2} \left( e_m (1 - m^2) + \tilde{r}_z \frac{de_m}{d\tilde{r}_z} \right) \right]} \quad (\text{B16})$$

This expression is evaluated at  $\tilde{r}_z = \sqrt{\Omega_0} z$ . The multiplicative factor at the front of Equation B16 is the acceleration profile of a simple harmonic oscillator, and the ratio of the sums captures the changing orbit shapes due to the Fourier distortion functions.

## REFERENCES

- |   |   |
|---|---|
| <p>Abdurro'uf, Accetta, K., Aerts, C., et al.<br/>2022, ApJS, 259, 35,<br/>doi: <a href="https://doi.org/10.3847/1538-4365/ac4414">10.3847/1538-4365/ac4414</a></p> | <p>Antoja, T., Helmi, A., Romero-Gómez, M.,<br/>et al. 2018, Nature, 561, 360,<br/>doi: <a href="https://doi.org/10.1038/s41586-018-0510-7">10.1038/s41586-018-0510-7</a></p> |
|---|---|

- Astropy Collaboration, Robitaille, T. P., Tollerud, E. J., et al. 2013, *A&A*, 558, A33, doi: [10.1051/0004-6361/201322068](https://doi.org/10.1051/0004-6361/201322068)
- Astropy Collaboration, Price-Whelan, A. M., Sipőcz, B. M., et al. 2018, *AJ*, 156, 123, doi: [10.3847/1538-3881/aabc4f](https://doi.org/10.3847/1538-3881/aabc4f)
- Astropy Collaboration, Price-Whelan, A. M., Lim, P. L., et al. 2022, *ApJ*, 935, 167, doi: [10.3847/1538-4357/ac7c74](https://doi.org/10.3847/1538-4357/ac7c74)
- Bahcall, J. N. 1984, *ApJ*, 287, 926, doi: [10.1086/162750](https://doi.org/10.1086/162750)
- Beaton, R. L., Oelkers, R. J., Hayes, C. R., et al. 2021, *AJ*, 162, 302, doi: [10.3847/1538-3881/ac260c](https://doi.org/10.3847/1538-3881/ac260c)
- Bédorf, J., Gaburov, E., Fujii, M. S., et al. 2014, in *Proceedings of the International Conference for High Performance Computing*, 54–65, doi: [10.1109/SC.2014.10](https://doi.org/10.1109/SC.2014.10)
- Bédorf, J., Gaburov, E., & Portegies Zwart, S. 2012, *Journal of Computational Physics*, 231, 2825, doi: [10.1016/j.jcp.2011.12.024](https://doi.org/10.1016/j.jcp.2011.12.024)
- Belokurov, V., Erkal, D., Evans, N. W., Koposov, S. E., & Deason, A. J. 2018, *MNRAS*, 478, 611, doi: [10.1093/mnras/sty982](https://doi.org/10.1093/mnras/sty982)
- Bennett, M., Bovy, J., & Hunt, J. A. S. 2022, *ApJ*, 927, 131, doi: [10.3847/1538-4357/ac5021](https://doi.org/10.3847/1538-4357/ac5021)
- Bertone, G., Hooper, D., & Silk, J. 2005, *PhR*, 405, 279, doi: [10.1016/j.physrep.2004.08.031](https://doi.org/10.1016/j.physrep.2004.08.031)
- Binney, J. 2012, *MNRAS*, 426, 1328, doi: [10.1111/j.1365-2966.2012.21692.x](https://doi.org/10.1111/j.1365-2966.2012.21692.x)
- Binney, J., & Tremaine, S. 2008, *Galactic Dynamics: Second Edition* (Princeton University Press)
- Binney, J., & Vasiliev, E. 2023, *arXiv e-prints*, arXiv:2306.11602, doi: [10.48550/arXiv.2306.11602](https://doi.org/10.48550/arXiv.2306.11602)
- Blondel, M., Berthet, Q., Cuturi, M., et al. 2021, *arXiv e-prints*, arXiv:2105.15183, doi: [10.48550/arXiv.2105.15183](https://doi.org/10.48550/arXiv.2105.15183)
- Bovy, J., Rix, H.-W., Liu, C., et al. 2012, *ApJ*, 753, 148, doi: [10.1088/0004-637X/753/2/148](https://doi.org/10.1088/0004-637X/753/2/148)
- Bovy, J., Rix, H.-W., Schlafly, E. F., et al. 2016, *ApJ*, 823, 30, doi: [10.3847/0004-637X/823/1/30](https://doi.org/10.3847/0004-637X/823/1/30)
- Bradbury, J., Frostig, R., Hawkins, P., et al. 2018, *JAX: composable transformations of Python+NumPy programs*, 0.3.13. <http://github.com/google/jax>
- Buch, J., Leung, J. S. C., & Fan, J. 2019, *JCAP*, 2019, 026, doi: [10.1088/1475-7516/2019/04/026](https://doi.org/10.1088/1475-7516/2019/04/026)
- Buckley, M. R., & Peter, A. H. G. 2018, *PhR*, 761, 1, doi: [10.1016/j.physrep.2018.07.003](https://doi.org/10.1016/j.physrep.2018.07.003)
- Buder, S., Lind, K., Ness, M. K., et al. 2022, *MNRAS*, 510, 2407, doi: [10.1093/mnras/stab3504](https://doi.org/10.1093/mnras/stab3504)
- Bullock, J. S., & Boylan-Kolchin, M. 2017, *ARA&A*, 55, 343, doi: [10.1146/annurev-astro-091916-055313](https://doi.org/10.1146/annurev-astro-091916-055313)
- Byrd, R. H., Lu, P., Nocedal, J., & Zhu, C. 1995, *SIAM Journal on Scientific Computing*, 16, 1190, doi: [10.1137/0916069](https://doi.org/10.1137/0916069)
- Cabezas, A., Lao, J., & Louf, R. 2023, *Blackjax: A sampling library for JAX*, 1.0.0. <http://github.com/blackjax-devs/blackjax>
- Chakrabarti, S., Chang, P., Lam, M. T., Vigeland, S. J., & Quillen, A. C. 2021, *ApJL*, 907, L26, doi: [10.3847/2041-8213/abd635](https://doi.org/10.3847/2041-8213/abd635)
- Dark Energy Survey Collaboration, Abbott, T., Abdalla, F. B., et al. 2016, *MNRAS*, 460, 1270, doi: [10.1093/mnras/stw641](https://doi.org/10.1093/mnras/stw641)
- Darragh-Ford, E., Hunt, J. A. S., Price-Whelan, A. M., & Johnston, K. V. 2023, *ApJ*, 955, 74, doi: [10.3847/1538-4357/acf1fc](https://doi.org/10.3847/1538-4357/acf1fc)
- de Jong, R. S., Agertz, O., Berbel, A. A., et al. 2019, *The Messenger*, 175, 3, doi: [10.18727/0722-6691/5117](https://doi.org/10.18727/0722-6691/5117)
- De Silva, G. M., Freeman, K. C., Bland-Hawthorn, J., et al. 2015, *MNRAS*, 449, 2604, doi: [10.1093/mnras/stv327](https://doi.org/10.1093/mnras/stv327)
- Eilers, A.-C., Hogg, D. W., Rix, H.-W., et al. 2022, *ApJ*, 928, 23, doi: [10.3847/1538-4357/ac54ad](https://doi.org/10.3847/1538-4357/ac54ad)
- Frankel, N., Hogg, D. W., & Price-Whelan, A. M. in prep.
- Freeman, K., & Bland-Hawthorn, J. 2002, *ARA&A*, 40, 487, doi: [10.1146/annurev.astro.40.060401.093840](https://doi.org/10.1146/annurev.astro.40.060401.093840)

- Gaia Collaboration, Prusti, T., de Bruijne, J. H. J., et al. 2016, *A&A*, 595, A1, doi: [10.1051/0004-6361/201629272](https://doi.org/10.1051/0004-6361/201629272)
- Gaia Collaboration, Katz, D., Antoja, T., et al. 2018, *A&A*, 616, A11, doi: [10.1051/0004-6361/201832865](https://doi.org/10.1051/0004-6361/201832865)
- Gaia Collaboration, Klioner, S. A., Mignard, F., et al. 2021, *A&A*, 649, A9, doi: [10.1051/0004-6361/202039734](https://doi.org/10.1051/0004-6361/202039734)
- Gaia Collaboration, Vallenari, A., Brown, A. G. A., et al. 2023, *A&A*, 674, A1, doi: [10.1051/0004-6361/202243940](https://doi.org/10.1051/0004-6361/202243940)
- Green, G. M., Ting, Y.-S., & Kamdar, H. 2023, *ApJ*, 942, 26, doi: [10.3847/1538-4357/aca3a7](https://doi.org/10.3847/1538-4357/aca3a7)
- Griffith, E. J., Hogg, D. W., Dalcanton, J. J., et al. 2023, arXiv e-prints, arXiv:2307.05691, doi: [10.48550/arXiv.2307.05691](https://doi.org/10.48550/arXiv.2307.05691)
- Harris, C. R., Millman, K. J., van der Walt, S. J., et al. 2020, *Nature*, 585, 357, doi: [10.1038/s41586-020-2649-2](https://doi.org/10.1038/s41586-020-2649-2)
- Hayden, M. R., Sharma, S., Bland-Hawthorn, J., et al. 2022, *MNRAS*, 517, 5325, doi: [10.1093/mnras/stac2787](https://doi.org/10.1093/mnras/stac2787)
- Helmi, A. 2020, *ARA&A*, 58, 205, doi: [10.1146/annurev-astro-032620-021917](https://doi.org/10.1146/annurev-astro-032620-021917)
- Helmi, A., Babusiaux, C., Koppelman, H. H., et al. 2018, *Nature*, 563, 85, doi: [10.1038/s41586-018-0625-x](https://doi.org/10.1038/s41586-018-0625-x)
- Hernquist, L. 1990, *ApJ*, 356, 359, doi: [10.1086/168845](https://doi.org/10.1086/168845)
- Hogg, D. W., Eilers, A.-C., & Rix, H.-W. 2019, *AJ*, 158, 147, doi: [10.3847/1538-3881/ab398c](https://doi.org/10.3847/1538-3881/ab398c)
- Holmberg, J., & Flynn, C. 2000, *MNRAS*, 313, 209, doi: [10.1046/j.1365-8711.2000.02905.x](https://doi.org/10.1046/j.1365-8711.2000.02905.x)
- Horta, D., Price-Whelan, A. M., Hogg, D. W., et al. 2023, arXiv e-prints, arXiv:2312.07664, doi: [10.48550/arXiv.2312.07664](https://doi.org/10.48550/arXiv.2312.07664)
- Hunt, J. A. S., Price-Whelan, A. M., Johnston, K. V., & Darragh-Ford, E. 2022, *MNRAS*, 516, L7, doi: [10.1093/mnrasl/slac082](https://doi.org/10.1093/mnrasl/slac082)
- Hunt, J. A. S., Stelea, I. A., Johnston, K. V., et al. 2021, *MNRAS*, 508, 1459, doi: [10.1093/mnras/stab2580](https://doi.org/10.1093/mnras/stab2580)
- Hunter, J. D. 2007, *Computing in Science & Engineering*, 9, 90, doi: [10.1109/MCSE.2007.55](https://doi.org/10.1109/MCSE.2007.55)
- Jin, S., Trager, S. C., Dalton, G. B., et al. 2023, *MNRAS*, doi: [10.1093/mnras/stad557](https://doi.org/10.1093/mnras/stad557)
- Khanna, S., Sharma, S., Tepper-Garcia, T., et al. 2019, *MNRAS*, 489, 4962, doi: [10.1093/mnras/stz2462](https://doi.org/10.1093/mnras/stz2462)
- Kollmeier, J. A., Zasowski, G., Rix, H.-W., et al. 2017, arXiv e-prints, arXiv:1711.03234, doi: [10.48550/arXiv.1711.03234](https://doi.org/10.48550/arXiv.1711.03234)
- Kuijken, K., & Gilmore, G. 1989a, *MNRAS*, 239, 571, doi: [10.1093/mnras/239.2.571](https://doi.org/10.1093/mnras/239.2.571)
- . 1989b, *MNRAS*, 239, 605, doi: [10.1093/mnras/239.2.605](https://doi.org/10.1093/mnras/239.2.605)
- . 1991, *ApJL*, 367, L9, doi: [10.1086/185920](https://doi.org/10.1086/185920)
- Laporte, C. F. P., Minchev, I., Johnston, K. V., & Gómez, F. A. 2019, *MNRAS*, 485, 3134, doi: [10.1093/mnras/stz583](https://doi.org/10.1093/mnras/stz583)
- Leung, H. W., & Bovy, J. 2019, *MNRAS*, 489, 2079, doi: [10.1093/mnras/stz2245](https://doi.org/10.1093/mnras/stz2245)
- Li, H., & Widrow, L. M. 2021, *MNRAS*, 503, 1586, doi: [10.1093/mnras/stab574](https://doi.org/10.1093/mnras/stab574)
- . 2023, *MNRAS*, 520, 3329, doi: [10.1093/mnras/stad244](https://doi.org/10.1093/mnras/stad244)
- Lian, J., Bergemann, M., Pillepich, A., Zasowski, G., & Lane, R. R. 2023, *Nature Astronomy*, 7, 951, doi: [10.1038/s41550-023-01977-z](https://doi.org/10.1038/s41550-023-01977-z)
- Lian, J., Zasowski, G., Mackereth, T., et al. 2022, *MNRAS*, 513, 4130, doi: [10.1093/mnras/stac1151](https://doi.org/10.1093/mnras/stac1151)
- LSST Science Collaboration, Abell, P. A., Allison, J., et al. 2009, arXiv e-prints, arXiv:0912.0201, doi: [10.48550/arXiv.0912.0201](https://doi.org/10.48550/arXiv.0912.0201)
- Maciel, W. J., & Quireza, C. 1999, *A&A*, 345, 629
- Magorrian, J. 2014, *MNRAS*, 437, 2230, doi: [10.1093/mnras/stt2031](https://doi.org/10.1093/mnras/stt2031)
- Majewski, S. R., Schiavon, R. P., Frinchaboy, P. M., et al. 2017, *AJ*, 154, 94, doi: [10.3847/1538-3881/aa784d](https://doi.org/10.3847/1538-3881/aa784d)
- Miyamoto, M., & Nagai, R. 1975, *PASJ*, 27, 533
- Navarro, J. F., Frenk, C. S., & White, S. D. M. 1997, *ApJ*, 490, 493, doi: [10.1086/304888](https://doi.org/10.1086/304888)

- Ness, M. K., Johnston, K. V., Blancato, K., et al. 2019, *ApJ*, 883, 177, doi: [10.3847/1538-4357/ab3e3c](https://doi.org/10.3847/1538-4357/ab3e3c)
- Nordström, B., Mayor, M., Andersen, J., et al. 2004, *A&A*, 418, 989, doi: [10.1051/0004-6361:20035959](https://doi.org/10.1051/0004-6361:20035959)
- Novara, A., Hogg, D. W., & Price-Whelan, A. M. in prep.
- Oort, J. H. 1932, *BAN*, 6, 249
- Peebles, P. J. E., Tully, R. B., & Shaya, E. J. 2011, arXiv e-prints, arXiv:1105.5596, doi: [10.48550/arXiv.1105.5596](https://doi.org/10.48550/arXiv.1105.5596)
- Price-Whelan, A. 2018, doi: [10.5281/zenodo.1228136](https://doi.org/10.5281/zenodo.1228136)
- . 2024, *adrn/TorusImaging: v0.1, v0.1*, Zenodo, doi: [10.5281/zenodo.10498412](https://doi.org/10.5281/zenodo.10498412)
- Price-Whelan, A. M. 2017, *The Journal of Open Source Software*, 2, doi: [10.21105/joss.00388](https://doi.org/10.21105/joss.00388)
- Price-Whelan, A. M., Hogg, D. W., Johnston, K. V., et al. 2021, *ApJ*, 910, 17, doi: [10.3847/1538-4357/abeb17](https://doi.org/10.3847/1538-4357/abeb17)
- Ramos, P., Antoja, T., & Figueras, F. 2018, *A&A*, 619, A72, doi: [10.1051/0004-6361/201833494](https://doi.org/10.1051/0004-6361/201833494)
- Ratcliffe, B. L., & Ness, M. K. 2023, *ApJ*, 943, 92, doi: [10.3847/1538-4357/aca8a1](https://doi.org/10.3847/1538-4357/aca8a1)
- Read, J. I. 2014, *Journal of Physics G Nuclear Physics*, 41, 063101, doi: [10.1088/0954-3889/41/6/063101](https://doi.org/10.1088/0954-3889/41/6/063101)
- Rix, H.-W., & Bovy, J. 2013, *A&A Rv*, 21, 61, doi: [10.1007/s00159-013-0061-8](https://doi.org/10.1007/s00159-013-0061-8)
- Sanders, J. L., & Binney, J. 2015, *MNRAS*, 449, 3479, doi: [10.1093/mnras/stv578](https://doi.org/10.1093/mnras/stv578)
- Santana, F. A., Beaton, R. L., Covey, K. R., et al. 2021, *AJ*, 162, 303, doi: [10.3847/1538-3881/ac2cbc](https://doi.org/10.3847/1538-3881/ac2cbc)
- Sharma, S., Hayden, M. R., Bland-Hawthorn, J., et al. 2021, *MNRAS*, 506, 1761, doi: [10.1093/mnras/stab1086](https://doi.org/10.1093/mnras/stab1086)
- Shaver, P. A., McGee, R. X., Newton, L. M., Danks, A. C., & Pottasch, S. R. 1983, *MNRAS*, 204, 53, doi: [10.1093/mnras/204.1.53](https://doi.org/10.1093/mnras/204.1.53)
- Spitzer, Lyman, J., & Schwarzschild, M. 1951, *ApJ*, 114, 385, doi: [10.1086/145478](https://doi.org/10.1086/145478)
- Taghizadeh-Popp, M., Kim, J., Lemson, G., et al. 2020, *Astronomy and Computing*, 33, 100412, doi: <https://doi.org/10.1016/j.ascom.2020.100412>
- Tian, H.-J., Liu, C., Wu, Y., Xiang, M.-S., & Zhang, Y. 2018, *ApJL*, 865, L19, doi: [10.3847/2041-8213/aae1f3](https://doi.org/10.3847/2041-8213/aae1f3)
- Toomre, A. 1964, *ApJ*, 139, 1217, doi: [10.1086/147861](https://doi.org/10.1086/147861)
- Vasiliev, E. 2019, *MNRAS*, 482, 1525, doi: [10.1093/mnras/sty2672](https://doi.org/10.1093/mnras/sty2672)
- Virtanen, P., Gommers, R., Oliphant, T. E., et al. 2020, *Nature Methods*, 17, 261, doi: [10.1038/s41592-019-0686-2](https://doi.org/10.1038/s41592-019-0686-2)
- Widmark, A., de Salas, P. F., & Monari, G. 2021, *A&A*, 646, A67, doi: [10.1051/0004-6361/202039852](https://doi.org/10.1051/0004-6361/202039852)
- Widmark, A., & Monari, G. 2019, *MNRAS*, 482, 262, doi: [10.1093/mnras/sty2400](https://doi.org/10.1093/mnras/sty2400)
- Widrow, L. M., & Dubinski, J. 2005, *ApJ*, 631, 838, doi: [10.1086/432710](https://doi.org/10.1086/432710)
- Yan, H., Li, H., Wang, S., et al. 2022, *The Innovation*, 3, 100224, doi: [10.1016/j.xinn.2022.100224](https://doi.org/10.1016/j.xinn.2022.100224)
- York, D. G., Adelman, J., Anderson, John E., J., et al. 2000, *AJ*, 120, 1579, doi: [10.1086/301513](https://doi.org/10.1086/301513)
- Yu, Z., Li, J., Chen, B., et al. 2021, *ApJ*, 912, 106, doi: [10.3847/1538-4357/abf098](https://doi.org/10.3847/1538-4357/abf098)
- Zasowski, G., Cohen, R. E., Chojnowski, S. D., et al. 2017, *AJ*, 154, 198, doi: [10.3847/1538-3881/aa8df9](https://doi.org/10.3847/1538-3881/aa8df9)